Energy Reports 13 (2025) 834–855

Contents lists available at ScienceDirect

Energy Reports

journal homepage: www.elsevier.com/locate/egyr

Research Paper

Optimising flywheel energy storage systems for enhanced windage loss reduction and heat transfer: A computational fluid dynamics and ANOVA-based approach

Mahmoud Eltaweel [a], Noha A. Mostafa [b,c], Christos Kalyvas [a], Yong Chen [a], Mohammad Reza Herfatmanesh [a,*]

[a] School of Physics, Engineering and Computer Science, University of Hertfordshire, Hatfield AL10 9AB, United Kingdom
[b] Industrial Engineering Department, Zagazig University, Zagazig, Sharkia 44519, Egypt
[c] Mechanical Engineering Department, The British University in Egypt, Shorouk City, Cairo 11837, Egypt

ARTICLE INFO

Keywords:
Analysis of variance
Flywheel energy storage systems
Taylor-Couette flow
Windage losses

ABSTRACT

Concerns about global warming and the need to reduce carbon emissions have prompted the creation of novel energy recovery systems. Continuous braking results in significant energy loss during urban driving. Flywheel energy storage systems (FESS) can recover and store vehicle kinetic energy during deceleration. In this work, Computational Fluid Dynamics (CFD) simulations have been carried out using the Analysis of Variance (ANOVA) technique to determine the effects of design parameters on flywheel windage losses and heat transfer characteristics. The influence of five parameters was studied: flywheel operating speed, radial airgap size, axial airgap size, rotor surface roughness and housing surface roughness. Two models were developed to assess the significance and effects of the studied parameters on windage losses and Nusselt number to determine the most optimal conditions. The significance and dependency of these parameters are investigated using the ANOVA technique. The ANOVA interaction analysis showed that all the studied parameters interact significantly. The results indicate that optimising the radial and axial airgap sizes led to a significant 19 % reduction in windage losses, while increasing the radial airgap significantly enhanced the Nusselt number by 33 %, thereby improving convective heat transfer. The study also found that increasing rotor and housing surface roughness improved heat dissipation, as observed by up to a 2.7 % increase in the Nusselt number. It was concluded that optimal configurations of radial radius ratio and axial radius ratio, in combination with targeted surface roughness, can lower rotor surface temperatures, reducing energy loss from frictional heating and enhancing the system's energy efficiency. The findings of this study can be used to develop guidelines for the design optimisation of FESS.

1. Introduction

The road transport sector accounts for one-fifth of global carbon dioxide emissions; most of these emissions come from passenger vehicles, which account for 45.1 % (Ritchie, 2023). By 2070, the International Energy Agency (IEA) predicts that global transportation will double, car ownership will rise by 60 %, and demand for passenger and freight aviation will triple ('Energy Technology Perspectives, 2020). One of the sources of energy inefficiency in road transportation is the loss of vehicle's kinetic energy during braking in the form of heat. One of the key enabling technologies to reduce emissions from passenger vehicles is regenerative braking. This technology allows for the vehicle's kinetic energy to be recovered and stored during deceleration and reused during acceleration (Lv et al., 2015). A vehicle's kinetic energy can be recovered and stored in a flywheel energy storage system (FESS) (Erhan and Özdemir, 2021); therefore, optimisation of flywheel design is critical to the advancement of flywheel development and the reduction of emissions (Olabi et al., 2021; Choudhary et al., 2012). Many requirements must be met by a flywheel design, such as safety factors, inertia energy, lifetime, space limit and support bearing (Li et al., 2022). Kale and Secanell (Kale and Secanell, 2018) conducted a comparative study of Metallic and fibre-reinforced composite material rotors for flywheels, employing mathematical models and optimisation to compare performance indices and introducing constraints to prevent radial tensile

* Corresponding author.
E-mail address: m.r.herfatmanesh@herts.ac.uk (M.R. Herfatmanesh).

https://doi.org/10.1016/j.egyr.2024.12.048
Received 17 May 2024; Received in revised form 15 December 2024; Accepted 16 December 2024
Available online 26 December 2024

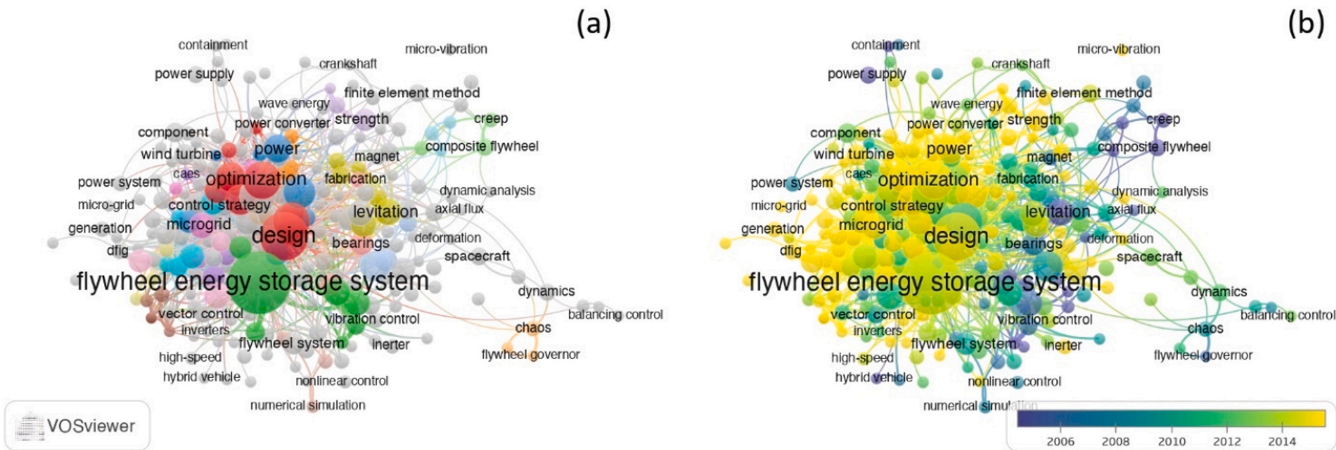

Fig. 1. Analysis of the keywords "Flywheel energy storage" from the web of science in VOS viewer. The search yielded 2241 papers as of May 2024. (a) The recurring topics are design, optimisation, control, power, etc. losses are not a recurring topic. (b) The time distribution shows that composite flywheel and vibration control are among the oldest topics, whereas design and optimisation are among the newest.

stresses in rotors. Metals are widely used to design a variety of flywheel shapes and sizes due to their low-cost, mature manufacturing and processing technologies (Kale and Secanell, 2018). The fibre-reinforced composite materials are anisotropic with high specific strength and can withstand sizeable circumferential stresses (Genta, 1985). However, metal rotors had a better energy per cost compared to composite rotors (Kale and Secanell, 2018).

Wang et al (Wang et al., 2021). enhanced electric vehicle braking by optimising a battery-flywheel system, improving energy recovery and stability while reducing battery charge currents. Mehraban et al (Mehraban et al., 2023a). analysed torque derivation and battery health in electric vehicles, focusing on conditions for optimal control system minimisation. Sun et al (Sun et al., 2022). optimised electromechanical flywheels for hybrid electric vehicles, enhancing energy efficiency. While Zhang et al (Zhang et al., 2023). introduced a novel flywheel hybrid electric powertrain that significantly improves vehicle performance, evidenced by over 50 % fuel economy enhancement and a 28.01 % increase in acceleration, while recovering up to 60.61 % of vehicle kinetic energy. Further, Mehraban et al (Mehraban et al., 2023b). showed that an AI-managed, optimally-sized, high-power-density energy storage system can mitigate power transients in electric vehicles, thereby extending battery life. Zhang et al (Zhang et al., 2020). proposed a variable inertia flywheel that enhances diesel generator speed stability by reducing sensitivity to loading impacts and improving system response and robustness, showing the diverse potential of flywheel technology.

Although flywheels are still relatively costly in automotive applications (Lukic et al., 2008), they are becoming more popular in automotive applications due to their higher power capacity and energy density compared to ultra-capacitors (Doucette and McCulloch, 2011). The main challenge facing flywheels is the high mechanical losses, such as bearing and windage losses (Amiryar and Pullen, 2020). Unlike the bearing loss, which is typically determined by factors such as flywheel weight and lubricant type, the windage losses can be reduced through modifications to the flywheel and the housing. Windage loss is caused by friction drag between the rotor and the surrounding air (Amiryar and Pullen, 2020). Given the flywheels' high peripheral speeds, the aerodynamic losses due to friction are relatively high. Losses arise not only because of skin friction but also because air moves radially outwards near the rotor. Therefore, it would not only lead to excessive energy loss but also excessive heat generation with the potential to overheat the rotor (Pullen and Dhand, 2014).

Suzuki et al (Suzuki et al., 2005). stated that using a mixture of 50 % helium and 50 % air as the working fluid inside the housing can reduce the aerodynamic losses by 43 % with a further increase in the helium concentration to 75 % resulting in more than 70 % reduction in the windage losses. Chiriţă et al. (2017) optimised a titanium alloy flywheel, with the outer diameter having the biggest impact on specific energy. Rim dimensions and disc thickness also influenced specific energy. Understanding windage losses in small-scale high-speed FESS drives this research to develop optimal flywheel design and operating conditions for high energy conversion efficiency. Nakane et al. (2016) proposed a method to reduce windage losses in high-speed electric motors. They experimented with different motor types and rotor structures, concluding that using a shrouded rotor significantly decreases windage losses while maximising torque, power, and motor efficiency in the high-speed zone. Pfister and Perriard, (2008) developed an optimisation model for a high-speed slotless permanent magnet motor. The model determined that an airgap size of 1.36 mm yielded the best performance, resulting in a power loss of 28 W with an 8.24 mm rotor radius. Magnetic fields, mechanical stresses, and various power losses were considered. Aydogmus et al. (2022) presented the design, optimisation, and analysis of a FESS used as a Dynamic Voltage Restorer, including the development and optimisation of a Permanent Magnet Synchronous Motor (PMSM) compatible with the matrix converter voltage level, achieved through a multi-objective optimisation algorithm.

FESS efficiency is obstructed by standby and windage losses due to aerodynamic drag in high-speed rotations. Studies using CFD and Analysis of Variance (ANOVA) have focused on optimising design elements like airgap size and rotor housing geometries. These enhancements aim to reduce power loss and improve system performance (Eltaweel and Herfatmanesh, 2023a, 2023b), Awad and Martin, (1997) studied windage losses on pulse generator rotors, finding that the skin friction coefficient depends on the Taylor Number for both the disc and cylinder sides. Kim et al. (2016) investigated the impact of airgap fans on induction motor cooling, showing that these fans increased flow rate distribution in the airgap and improved overall winding cooling performance by 55 % on average, with significant enhancements in heat transfer coefficients. Wang et al. (2022) developed a control strategy for High-Speed Motor-Flywheel Energy Storage Systems (HSM-FESS), with simulation models confirming the effectiveness of their approach. Furthering control mechanisms, Jia et al. (2022) outlined a control strategy that ensures stability and enhanced power output of FESS under low voltage conditions. Zhang et al. (2022) extended this discussion by reviewing various FESS control strategies and presenting a comparative study of converter types, providing a broad spectrum of applications.

A detailed review of FESS trends and research directions, such as those highlighted by Li and Palazzolo, (2022) and Bamisile et al. (2023)

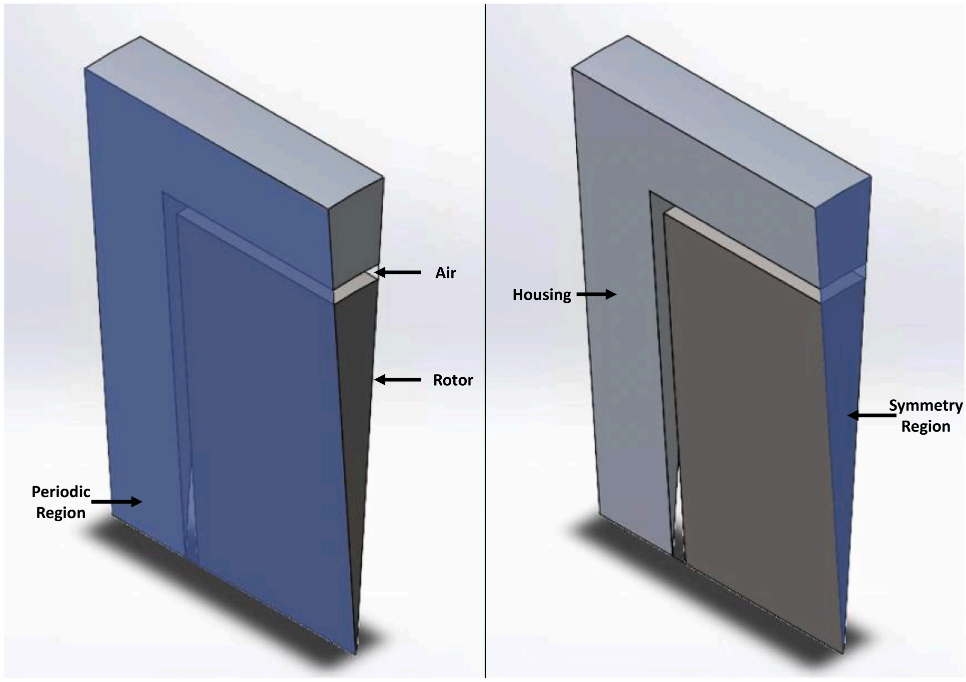

Fig. 2. The FESS computational domain.

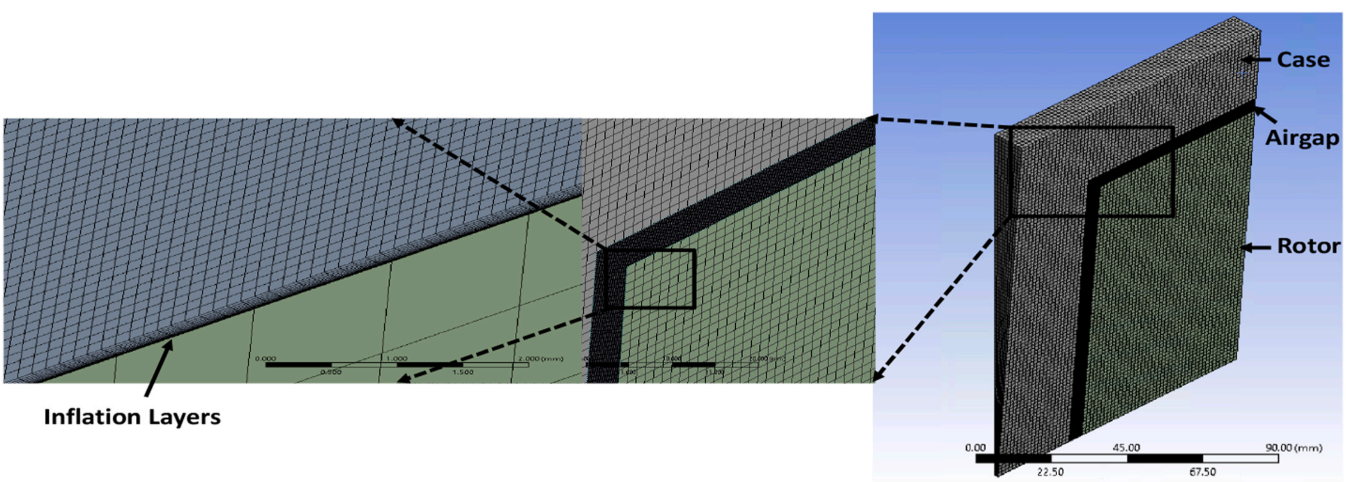

Fig. 3. The quadrilateral mesh used to model the FESS.

reveals a lack of studies addressing frictional windage losses in the existing literature. As illustrated in Fig. 1, a representation map of the keywords "Flywheel energy storage" from the Web of Science search engine shows that "losses" rarely emerge as a primary focus. Most prior studies have concentrated on design, control, bearing characteristics, and general optimisation approaches without delving into multi-parameter statistical optimisation for factors such as axial airgap size or the interactions between rotor and housing SR and airgap dimensions. Addressing these limitations, this study contributes a novel statistical approach to FESS optimisation, focusing on complex parameter interactions previously unexplored in the literature and advancing FESS design for enhanced energy efficiency and reduced operational losses.

Several Research Questions (RQs) were addressed in this work:

RQ1 What are the challenges of optimising the performance of Flywheel energy storage systems?

RQ2 What is the influence of different key parameters on the performance of the system?

RQ3 What are the combined effects of multiple critical parameters including operating speed, radial and axial airgap sizes, and surface roughness on windage losses and heat transfer within the system?

RQ4 How to identify the optimal parameter combinations and investigate their interaction impact on FESS efficiency?

Optimising the performance of FESS requires a comprehensive understanding of the influence of key rotor design parameters, particularly airgap size, operating speed, and surface roughness (SR). This study addresses these optimisation challenges by examining the combined effects of multiple critical parameters including operating speed, radial and axial airgap sizes, and SR on windage losses and heat transfer within FESS. Through Analysis of Variance (ANOVA), this research identifies optimal parameter combinations and investigates how these parameters interact to impact FESS efficiency. The novelty of this work is evaluating the combined influence of surface roughness on both the rotor and housing, analysing the specific effect of axial airgap size, and assessing

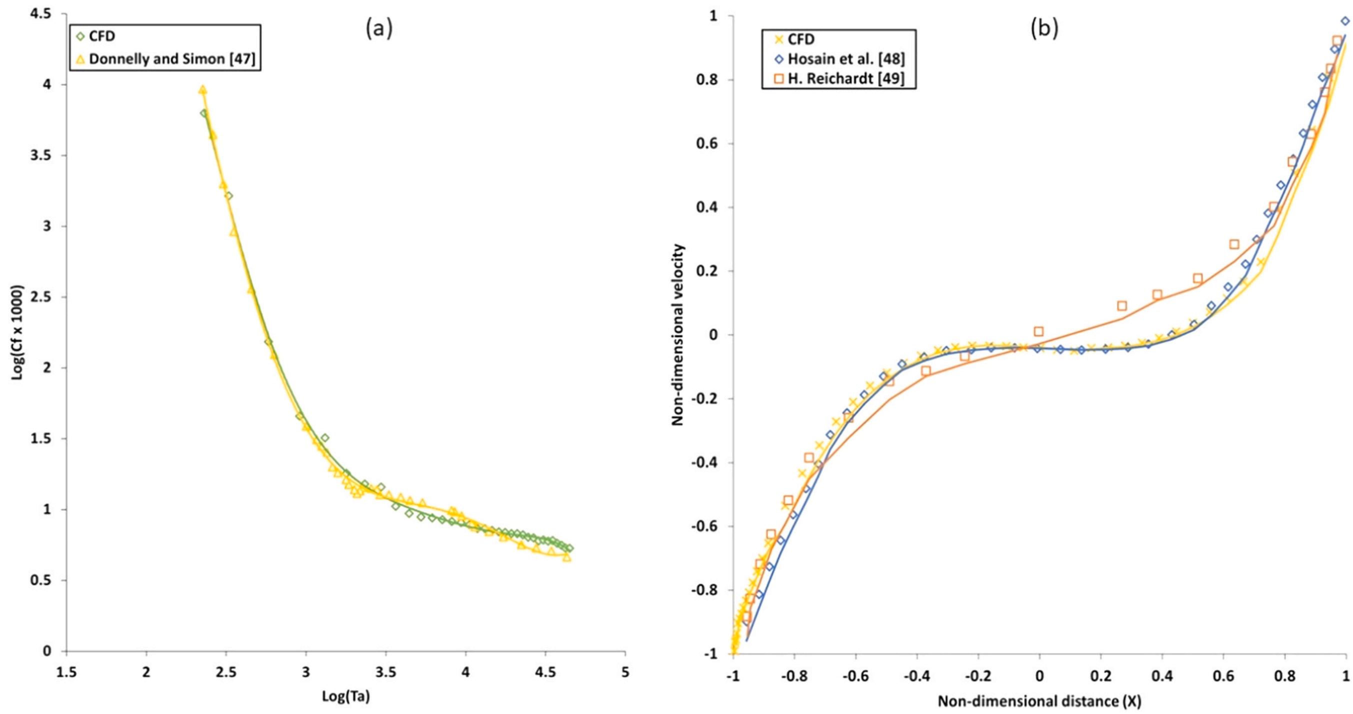

Fig. 4. The validation of (a) rotor skin friction coefficient as a function of Taylor number, (b) average velocity profile within the airgap.

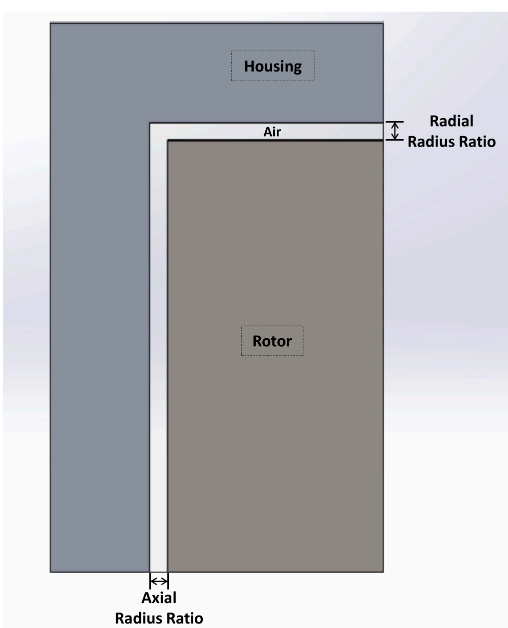

Fig. 5. The simplified FESS geometry.

the interaction between axial and radial airgap sizes within a thorough optimisation framework. Hence, covering an existing gap in the literature.

2. Flow characterisation

The flow in the annulus of concentric cylinders with a rotating inner cylinder and a stationary outer cylinder (similar to FESS) is commonly known as Couette flow which occurs when two parallel surfaces, separated by a fluid, move in a steady and relative motion (Rohsenow et al., 1998). At high rotating speeds, centrifugal instability leads to the

Table 1
FESS factors studied.

Levels	Factors				
	A Radial Radius Ratio [RRR]	B Axial Radius Ratio [ARR]	C Housing Surface Roughness (m) [HSR]	D Rotor Surface Roughness (m) [RSR]	E Rotational Speed (rad/s)
1	0.99	0.99	0	0	200
2	0.98	0.98	5e−6	5e−7	800
3	0.97	0.97	5e−5	5e−6	1600
4	0.96	0.96	1e−4	5e−5	2400

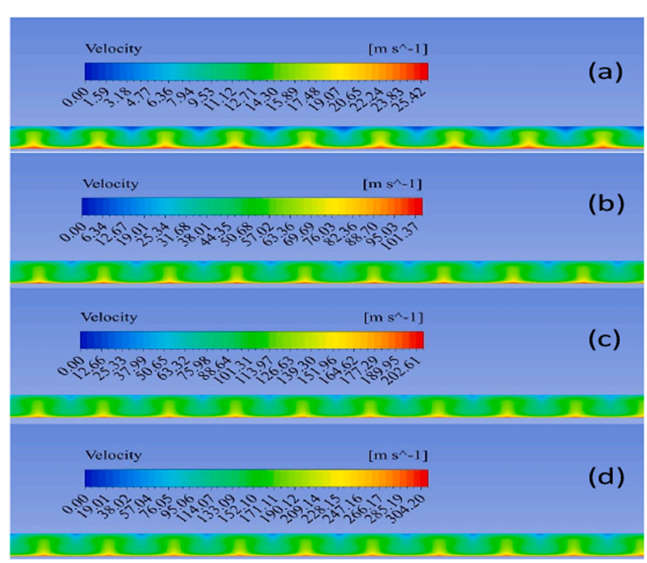

Fig. 6. Air velocity distribution within the airgap with RR of 0.99 at different rotational speeds: (a) 200 rad/s, (b) 800 rad/s, (c) 1600 rad/s, (d) 2400 rad/s.

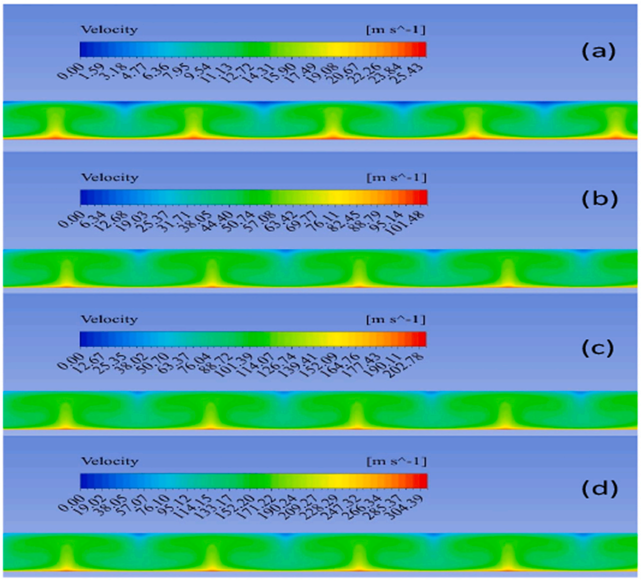

Fig. 7. Air velocity distribution within the airgap with RR of 0.98 at different rotational speeds: (a) 200 rad/s, (b) 800 rad/s, (c) 1600 rad/s, (d) 2400 rad/s.

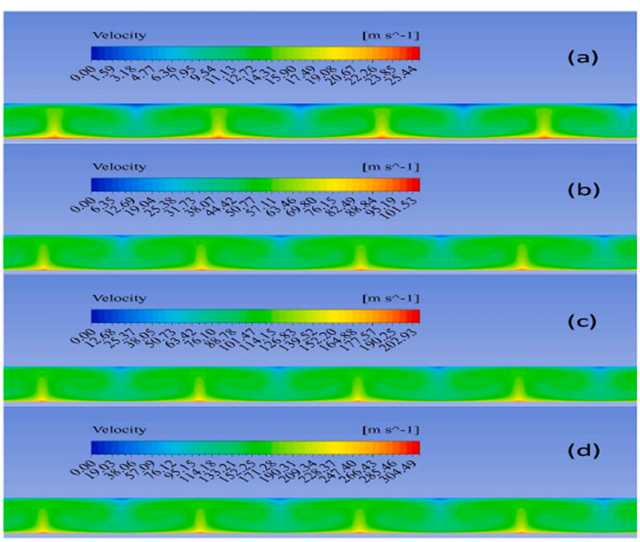

Fig. 8. Air velocity distribution within the airgap with RR of 0.97 at different rotational speeds: (a) 200 rad/s, (b) 800 rad/s, (c) 1600 rad/s, (d) 2400 rad/s.

formation of circumferential Taylor vortices in the airgap (Childs, 2010). The air velocity field, influenced by tangential airflow and Taylor-Couette flow, determines the level of windage losses. To calculate these losses, the airflow within the airgap is analysed. The power required to overcome windage losses in a rotating cylinder can be determined using Eq. (1) (Liu et al., 2003).

$$P_w = (M_D + M_c)\omega \tag{1}$$

Where ω is the rotational velocity of the rotor, M_D is the disc moment on the side and M_c is the rotor moment which can be calculated using Eqs. (2) and (3), respectively (Liu et al., 2003).

$$M_D = \rho\omega^2 {r_o}^5 C_m \tag{2}$$

$$M_c = \pi\rho\omega^2 {r_o}^4 L C_w \tag{3}$$

Where ρ is the fluid density, L is the rotor length, r_o is the rotor radius, C_m

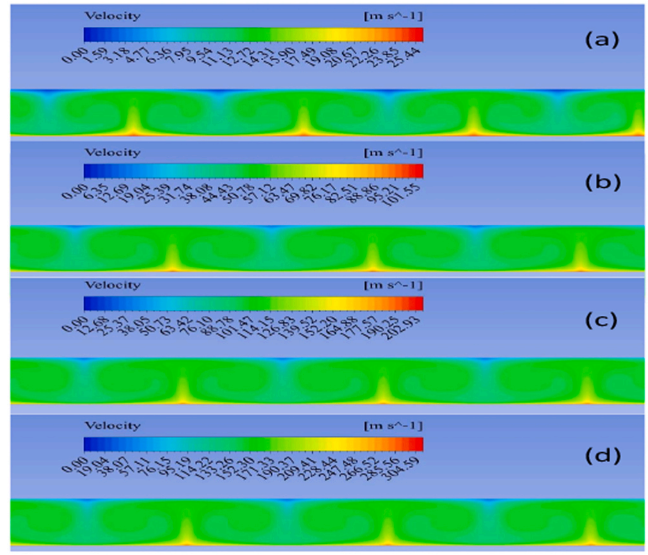

Fig. 9. Air velocity distribution within the airgap RR of 0.96 at different rotational speeds: (a) 200 rad/s, (b) 800 rad/s, (c) 1600 rad/s, (d) 2400 rad/s.

Table 2
ANOVA for response surface quadratic model for Nusselt number.

Source	Sum of Squares	df	Mean Square	F-value	p-value
A-RRR	19.77	1	19.77	7241.96	< 0.0001
B-ARR	42.27	1	42.27	15484.58	< 0.0001
C-RSR	0.1836	1	0.1836	67.26	< 0.0001
D-HSR	0.0459	1	0.0459	16.82	< 0.0001
E-Rotational Velocity	11.72	1	11.72	4293.87	< 0.0001
AB	4.60	1	4.60	1686.89	< 0.0001
AC	0.0315	1	0.0315	11.53	0.0007
AE	0.6975	1	0.6975	255.53	< 0.0001
BC	0.0639	1	0.0639	23.39	< 0.0001
BD	0.0377	1	0.0377	13.81	0.0002
BE	0.0203	1	0.0203	7.45	0.0065
CD	0.0265	1	0.0265	9.73	0.0019
CE	0.4035	1	0.4035	147.80	< 0.0001
DE	0.0528	1	0.0528	19.33	< 0.0001
A^2	0.2469	1	0.2469	90.46	< 0.0001
B^2	0.1122	1	0.1122	41.11	< 0.0001
D^2	0.1285	1	0.1285	47.06	< 0.0001
E^2	13.68	1	13.68	5011.73	< 0.0001
Residual	2.01	738	0.0027		
Total	121.47	756			

is the disc torque coefficient and C_w is the rotor skin friction coefficient.

Zero axial flow in an enclosed cylinder breaks down the laminar flow between the cylinders at specific angular velocities, creating a row of circumferential Taylor vortices (Taylor, 1923). If the clearance of the cylinder airgap is relatively small compared to the cylinder radius, the stable flow depends on the Taylor number, given by Eq. (4) (Reinke et al., 2018).

$$T_a = \frac{\omega \times r_o \times g}{\upsilon}\left(\frac{g}{r_o}\right)^{0.5} \tag{4}$$

Where r_o is the cylinder radius (rotor), g is the radial airgap width and υ is the kinematic viscosity. Taylor number can be used to determine the flow characteristics as shown by case Eq. (5) (Reinke et al., 2018).

$$If \begin{cases} T_a < 41.3 \mathit{Laminar\ Couettw\ flow} \\ 41.3 < T_a < 400 \mathit{Laminar\ flow\ with\ cellular\ Taylor\ vortices} \\ T_a > 400 \mathit{Turbulent\ flow} \end{cases} \tag{5}$$

Table 3
ANOVA for response surface quadratic model for windage losses.

Source	Sum of Squares	df	Mean Square	F-value	p-value
A-RRR	0.6483	1	0.6483	945.78	< 0.0001
B-ARR	0.0494	1	0.0494	72.06	< 0.0001
C-RSR	1.59	1	1.59	2318.62	< 0.0001
D-HSR	0.8097	1	0.8097	1181.28	< 0.0001
E-Rotational Velocity	672.74	1	672.74	9.8E+ 05	< 0.0001
AB	0.0035	1	0.0035	5.07	0.0246
AC	0.0255	1	0.0255	37.25	< 0.0001
AD	0.3429	1	0.3429	500.26	< 0.0001
AE	0.0327	1	0.0327	47.76	< 0.0001
BD	0.0029	1	0.0029	4.17	0.0414
CE	0.0189	1	0.0189	27.57	< 0.0001
DE	0.0100	1	0.0100	14.52	0.0002
B^2	0.0117	1	0.0117	17.09	< 0.0001
C^2	0.0861	1	0.0861	125.62	< 0.0001
D^2	0.0099	1	0.0099	14.41	0.0002
E^2	31.78	1	31.78	46371.62	< 0.0001
Residual	0.5148	751	0.0007		
Total	957.49	767			

Table 4
The fit statistics for the obtained initial response.

First Response	Std. Dev.	0.0522	R^2	0.9834
	Mean	3.18	**Adjusted R^2**	0.9830
	C.V.%	1.64	**Predicted R^2**	0.9825
			Adequate Precision	219.7237
Second Response	**Std. Dev.**	0.0262	**R^2**	0.9995
	Mean	6.66	**Adjusted R^2**	0.9995
	C.V.%	0.3933	**Predicted R^2**	0.9994
			Adequate Precision	768.5666

3. Numerical modelling

In this study, we utilised a combined Computational Fluid Dynamics (CFD) and Analysis of Variance (ANOVA) approach within the Design of experiment (DoE) framework, functioning as a statistical tool to analyse factor significance and interactions. This approach enabled a highly detailed analysis of the effects and interactions of multiple FESS parameters, including airgap sizes, surface roughness, and operating speed. This combination allowed us to identify specific parameter effects and their interactions, which is essential for accurately modelling and optimising windage losses and heat transfer in FESS. The following subsections outline the governing equations, mesh generation, boundary conditions, and validation processes.

3.1. Governing equations and assumptions

This study aims to develop a numerical model of a FESS assuming a smooth, narrow and closed design. CFD is used to model the airgap flow structure and predict the skin friction coefficient. The latter is determined based on the velocity distribution within the airgap. The governing equations used by the CFD code are based on fluid motion conservation equations (Andersson et al., 2011). In this study, the CFD domain of an enclosed FESS is created, where the domain is divided into computational cells and nodes. The governing equations are numerically discretised into a system of linear algebraic equations using a finite volume method after the mesh is created (Tu et al., 2008). The conservation of mass in fluid flow is articulated by the continuity equation, as delineated in Eq. (6) (Andersson et al., 2011).

$$\frac{\partial \rho}{\partial t} + \nabla.\rho V = 0 \tag{6}$$

Newton's second law for fluid mechanics postulates that the rate of

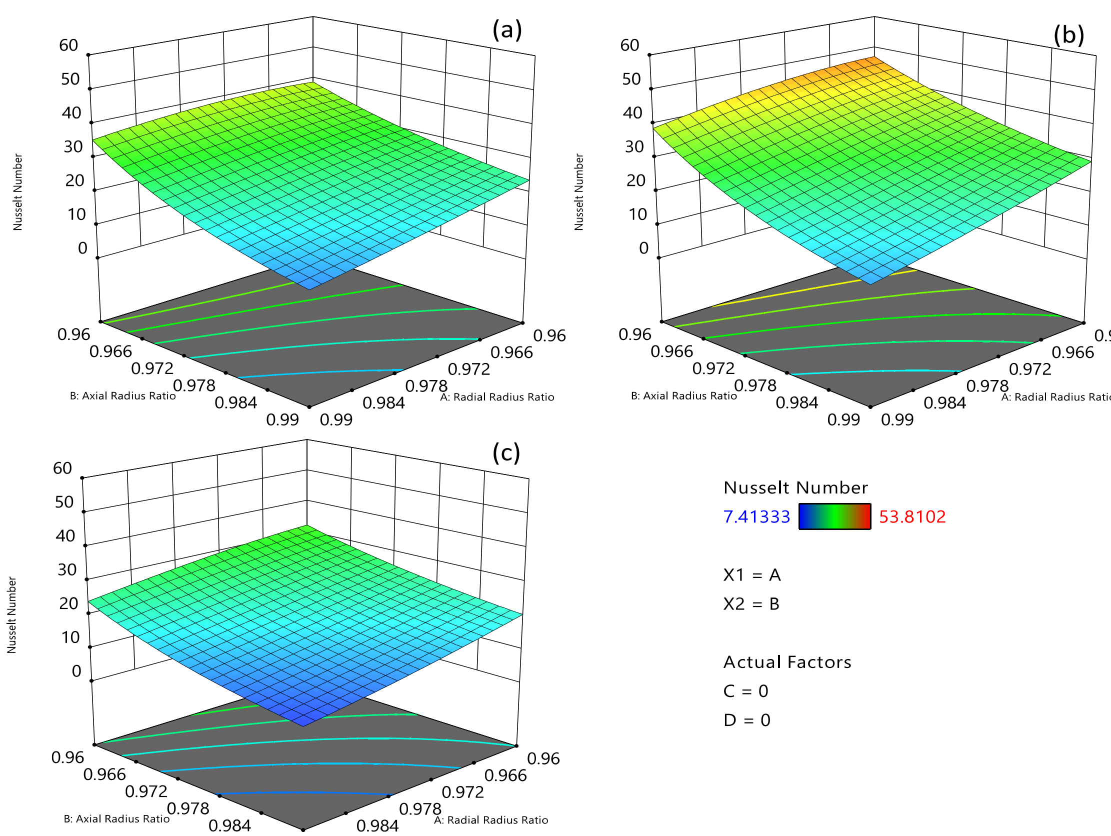

Fig. 10. 3D plot of Nusselt number as a function of RRR and ARR at different rotational speeds: (a) 800 rad/s, (b) 1600 rad/s, (c) 2400 rad/s.

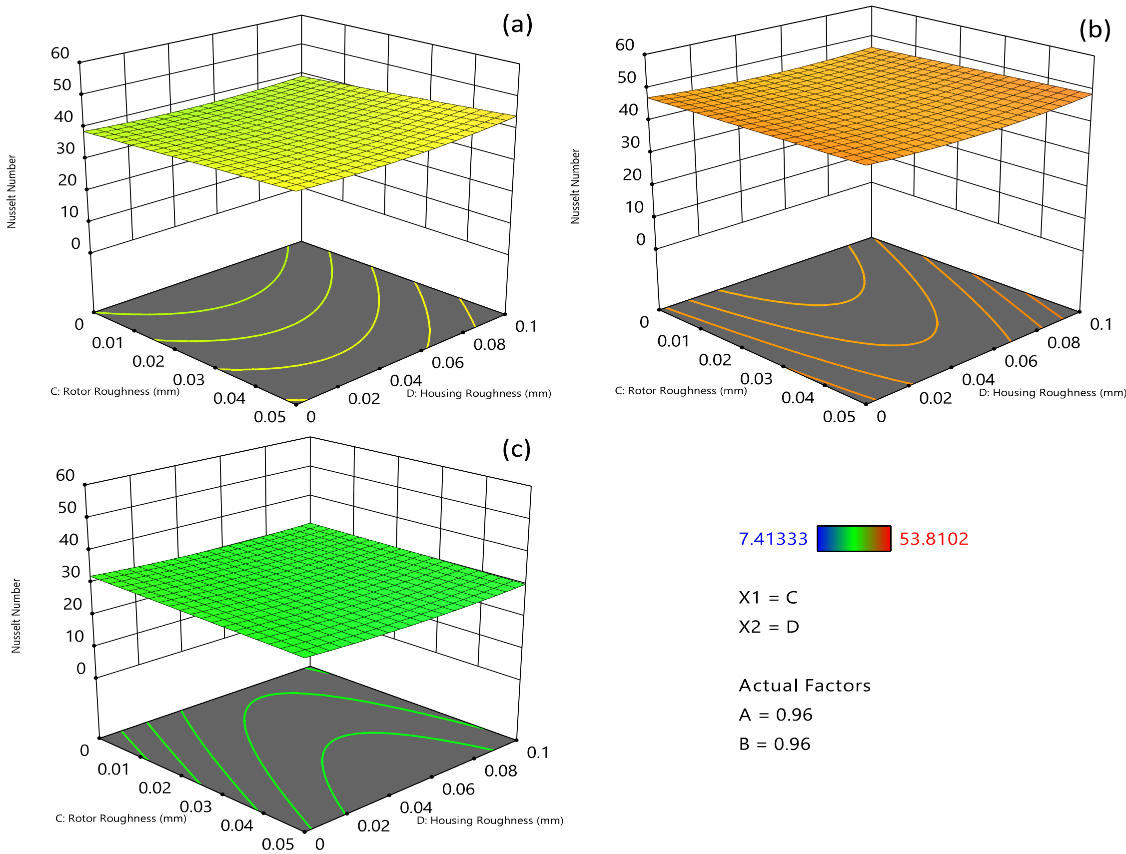

Fig. 11. 3D plot of Nusselt number as a function of RSR and HSR at different rotational speeds: (a) 800 rad/s, (b) 1600 rad/s, (c) 2400 rad/s.

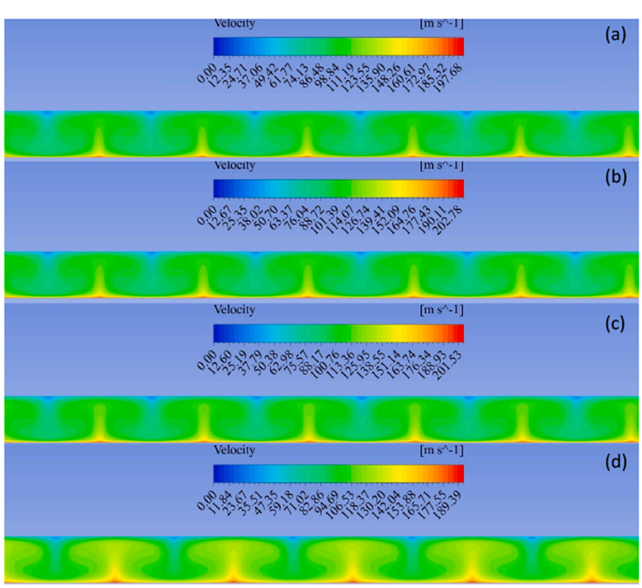

Fig. 12. Air velocity distribution within the airgap at 1600 rad/s for RRR and ARR of 0.98 at different RSR heights: (a) Ks= 0, (b) Ks= 5e-7 m, (c) Ks= 5e-6 m, (d) Ks= 5e-5 m.

momentum change in a fluid particle is equivalent to the aggregate forces acting upon said particle, as depicted in Eq. (7) (Tu et al., 2008).

$$\frac{D(\rho V)}{Dt} = -\nabla p + \nabla \bullet \tau_{ij} + \rho g \tag{7}$$

Eq. (8) provides the foundation for deriving the energy equation pertinent to a compressible, viscous Newtonian fluid flow (Tu et al., 2008).

$$\frac{D(\rho C_p T)}{Dt} = \nabla \bullet (\lambda \nabla T) + \Phi \tag{8}$$

Where V is the velocity vector, ∇p is the pressure force, $\nabla \bullet \tau_{ij}$ is the viscous force, ρg is the gravitational force, $\nabla \bullet (\lambda \nabla T)$ is the heat conduction through the fluid element boundaries, λ is the thermal conductivity, T is the temperature and Φ is the heat from the conversion of mechanical energy.

3.2. Mesh generation and boundary conditions

The CFD software used in this study is ANSYS Fluent 19R2. The parameters used in this study to define the airgap are η, a dimensionless parameter referred to as the radius ratio (RR) where $\eta = r_o/r_h$ and the aspect ratio $\Gamma = L/g$. The radius and the rotor length were chosen to be 0.13 m. RRs of 0.99, 0.98, 0.97 and 0.96 have been investigated, corresponding to airgap size of 1.3 mm, 2.6 mm, 4 mm and 5.4 mm and aspect ratios of 100, 50, 32.5 and 24, respectively. Due to the symmetrical nature of the FESS geometry, the CFD domain was reduced to an 8-degree segment with a symmetry plane in the middle which significantly reduced the computational time, as illustrated in Fig. 2.

A structured quadrilateral mesh was used to model the FESS. Different mesh sizes were selected for mesh independence analysis; airgap sizes of 0.1 mm, 0.15 mm and 0.2 mm and the rotor and housing sizes of 1 mm, 1.5 mm and 2 mm. The objective was to identify the optimal mesh for the simulations by conducting a mesh independence test using the skin friction coefficient and the Nusselt number, as the parameters of interest, at the highest rotational speed of 2400 rad/s. Mesh independence was performed for a range of total mesh elements of 1.5 million to 6.5 million, with a total mesh element of 4.5 million

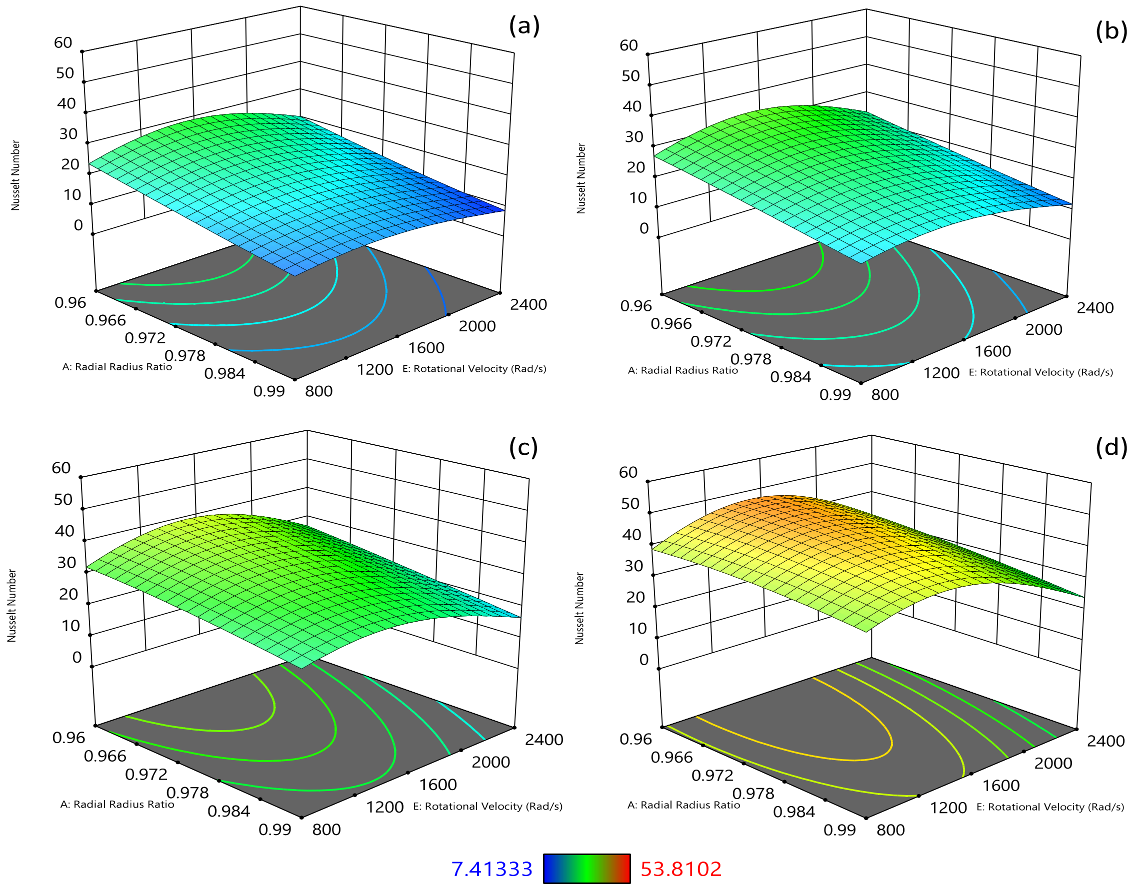

Fig. 13. 3D plot of Nusselt number as a function of RRR and rotational velocity at different ARRs: (a) 0.99, (b) 0.98, (c) 0.97, (d) 0.96.

selected as the optimum based on computational time and accuracy. The optimal mesh combination used in this study is shown in Fig. 3.

CFD simulations were used to investigate the aerodynamic performance of the FESS under steady-state conditions. A moving reference frame (MRF) is used to model time-averaged steady-state solutions for the rotor's relative motion. This method is suitable for steady-state analysis and can resolve most flow characteristics such as mass flow rate and pressure changes across rotating components (Anderson and Wendt, 1995). The SST K-ω turbulence model was used to solve Reynolds averaged Navier-Stokes (RANS) equations since the Reynolds number in the airgap indicated a turbulent flow regime for all the studied rotational speeds (Anderson et al., 2015; Howey et al., 2011; Jungreuthmayer et al., 2011). Based on a review of the existing literature for turbulence modelling of Taylor-Couette flow within concentric cylinders, the SST K-ω turbulence model is shown to be adequate for estimating fluid flow and heat transfer within the annulus of concentric cylinders (Nachouane et al., 2016; Jungreuthmayer et al., 2011). The following assumptions have been made for the numerical analysis:

- The effect of Gravity was ignored.
- Air was assumed to be an ideal gas.
- Thermal conductivity and specific heat remained constant.
- The system has no inlet or outlet.
- The thermal boundary condition of the housing was set to a free stream temperature of 24°C and heat transfer coefficients of 30 W/m^2.K.
- The initial temperature of all the system components was set to 24°C.

Since turbulence models are limited in their ability to capture the flow behaviour in the viscous region of the boundary layer, a high-resolution boundary layer mesh was generated using wall cells where the $y_+ \leq 1$. This allowed for accurate resolution of the viscous sublayer. Numerical discretisation of the governing equations was carried out using a finite volume method to solve a linear algebraic equation system for each cell. The second-order upwind discretisation scheme was used to simultaneously solve the governing.

3.3. Validation

The skin friction coefficient variation as a function of Taylor number was compared to experimental data presented by Donnelly (Donnelly, 1958) where the RR was similar to the value used in this study. Fig. 4a depicts the skin friction coefficient as a function of Taylor number. There are three distinct zones; the first is when the flow is laminar with no vortices, the second is laminar flow with Taylor-Couette vortices, which can be referred to as non-linear theory due to the non-linear aspect of the skin friction coefficient distribution and the third zone is turbulent flow in which the confined air is thoroughly mixed. The numerically obtained Taylor numbers are in good agreement with the values previously reported by Donnelly and Simon, (1960) Furthermore, when Taylor vortices form in the airgap, the skin friction coefficients estimated by the CFD model match the results reported by Donnelly and Simon, (1960) where the CFD calculations accurately reproduce the distribution of skin friction coefficient in the first zone.

In Fig. 4b, the simulated average velocity profile is presented alongside experimental data obtained from previous studies conducted by Hosain et al. (2017) and Reichardt, (1956). To ensure a fair comparison, the simulated values have been scaled to match the range of the experimental results. The non-dimensional coordinates $X = -1$ and $X = 1$ in Fig. 4b correspond to the housing and rotor wall, respectively. At low Reynolds numbers, the velocity profile exhibits a linear trend. However, for high Reynolds numbers, the velocity profile displays a

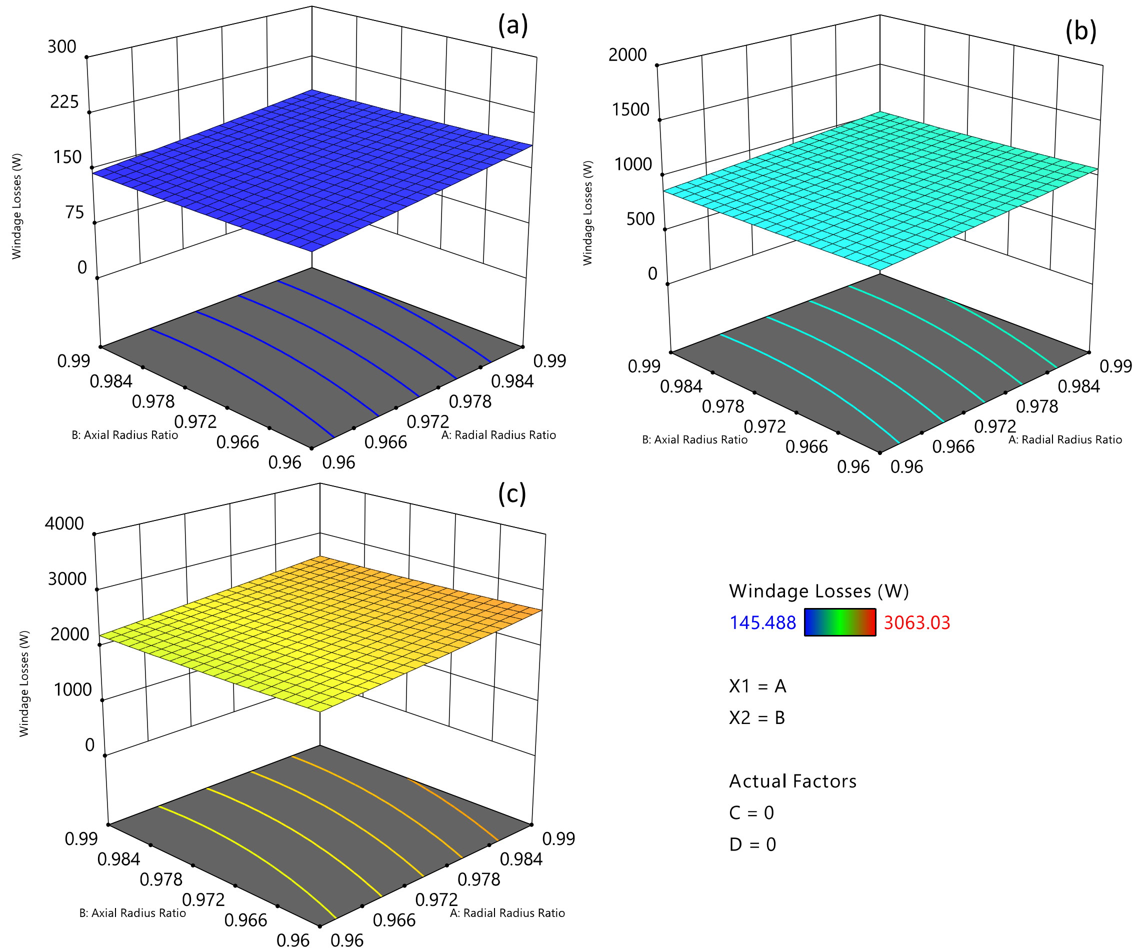

Fig. 14. 3D plot of windage losses as a function of RRR and ARR at different rotational speeds: (a) 800 rad/s, (b) 1600 rad/s, (c) 2400 rad/s.

steeper gradient near the walls due to the influence of viscous forces. The average velocity, in this case, is observed to occur at the midpoint of the airgap. The simulated average velocity profile is found to be in good agreement with the experimental velocity profiles, with similar patterns being reported in previous studies (Tatsumi, 2000; Aoki et al., 1967). In addition, the presented CFD model has been validated by the authors' previous experimental work (Motaman et al., 2023). The experimental and numerical results are in good agreement, with both methods exhibiting similar trends. The differences between experimental and numerical results are within a 15 % margin of error.

4. Parametric study

Analysis of variance (ANOVA) is a statistical tool that can be used to gain information about the relations between several variables the effects of each variable on the experiment and the interaction between them (Scheffe, 1999). The ANOVA technique identifies the significance of several FESS geometrical and operational parameters and their effects on reducing windage losses while maintaining maximum kinetic energy storage capacity and optimal heat transfer performance.

4.1. Responses selection

The system responses are selected to demonstrate the response surface's local form by simulating the interaction and quadratic effects of the system parameters. They are also used to assess the system's strengths and weaknesses and determine the optimal system settings. Two responses are examined in this model: Nusselt number and Windage loss. The Nusselt number is the crucial factor in determining the convection heat transfer inside the airgap and how it is affected by the design parameters. The increase in the Nusselt number will improve the heat transfer by convection, reducing the rotor temperature and the need for an internal cooling device while allowing for higher rotational velocities, which could increase the kinetic energy storage capacity. In addition, the windage loss, a crucial factor in determining the frictional losses of a FESS which, is responsible for the self-discharge rate of the FESS.

4.2. Factors selection

Several factors influence the FESS performance, in this study the effects of rotor and housing SR, rotational velocity and the radial and axial airgap sizes, shown in Fig. 5, have been considered. Since the overall size of the FESS is an important factor in various applications, four different sizes have been selected to create a narrow airgap size. The rotational velocity of the rotor was set to 2400 rad/s, which is the maximum allowable velocity of a solid steel cylindrical rotor with a safety factor of two (Han et al., 2012).

Surface roughness is the physical parameter used to characterise surface irregularities which impacts drag, heat and mass transfer on walls (Kadivar et al., 2021). Despite its presence in heterogeneous structures such as the FESS rotor and housing, its effect on windage losses has rarely been discussed in the literature. Two parameters define SR; the first is the roughness constant, a parameter that measures the uniformity of the roughness. Inputs can range from 0.5 to 1, where 0.5 indicates uniform wall roughness and 1 indicates strongly non-uniform roughness in terms of spacing and height. A value of 0.5 for the roughness constant was selected to ensure uniformity of wall roughness.

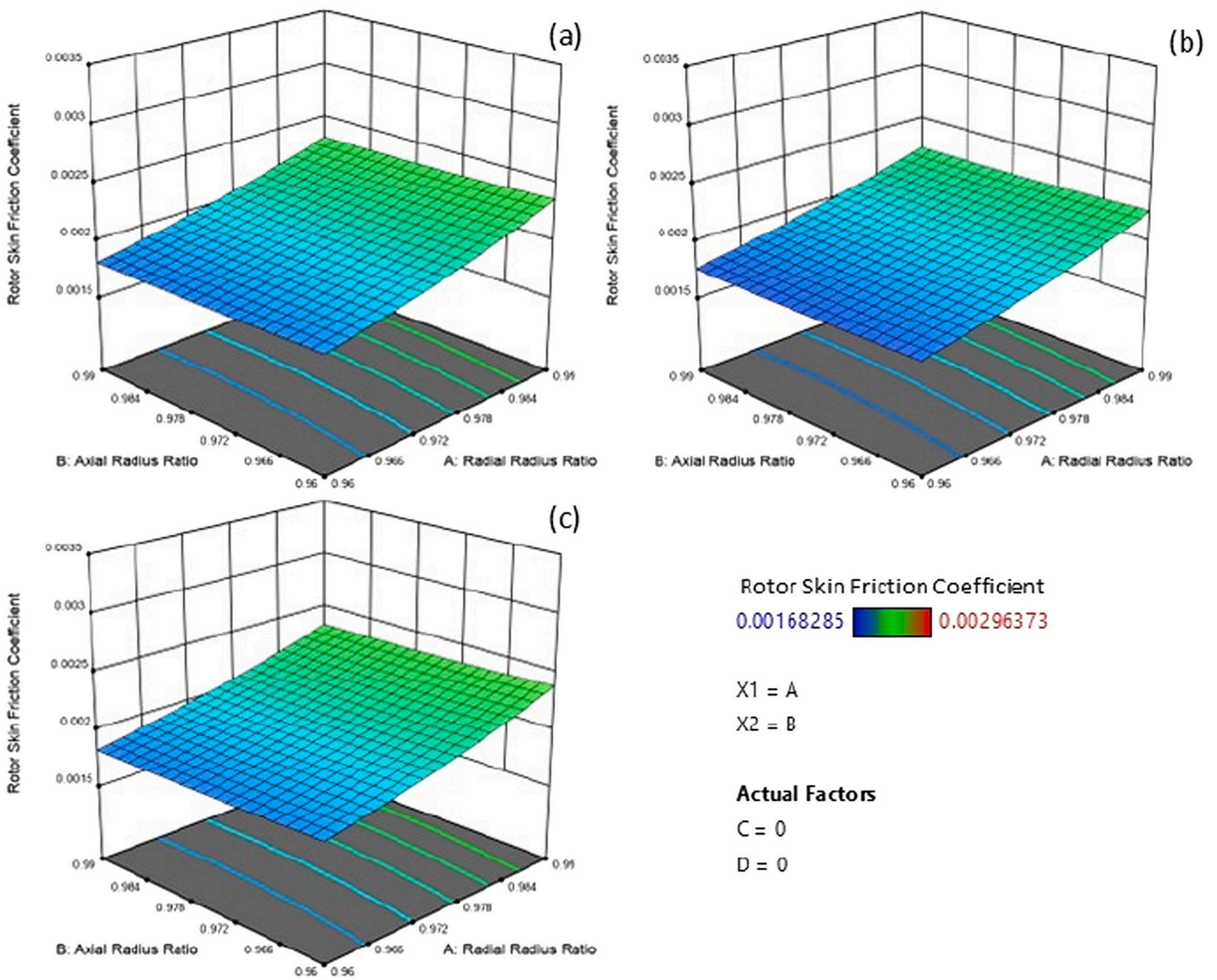

Fig. 15. 3D plot of rotor skin friction coefficient as a function of RRR and ARR at different rotational speeds: (a) 800 rad/s, (b) 1600 rad/s, (c) 2400 rad/s.

The second parameter is the physical roughness height; its default value is zero, corresponding to a smooth wall. A dimensionless roughness height can be calculated by Eq. (9) (Nachouane et al., 2016).

$$K_s^+ = \frac{K_s C_\mu^{0.25} k^{0.5}}{\upsilon} \tag{9}$$

Where K_s is the roughness height, C_μ is the turbulence model constant, equal to 0.0845 and k is the turbulent kinetic energy. Depending on the value of K_s^+, the flow regime can be categorised into three regions as shown by case Eq. (10) (Nachouane et al., 2016).

$$If \begin{cases} K_s^+ \le 2.25 \textit{Hydrodynamically smooth} \\ 2.25 \le K_s^+ \le 90 \textit{Transitional} \\ K_s^+ > 90 \textit{Fully rough} \end{cases} \tag{10}$$

In the hydrodynamically smooth region, roughness effects can be ignored, but they become increasingly important in the transitional and fully rough regimes (Nachouane et al., 2016). The dimensionless roughness height remained below 90 in all the tested cases in this study, indicating the flow regime to be either hydrodynamically smooth or transitional. The roughness values were chosen based on the selected materials: steel 4340 for the rotor and aluminium for the housing. Starting with a smooth surface ($K_s = zero$), another two roughness values were selected to be in the transitional region with K_s^+ greater than 2.25 (Abbas et al., 2022; Wen and Mudawar, 2006). While the effect of rotor SR has been previously studied by other researchers, to the best of the authors' knowledge, the combined effect of rotor and housing SR with the effect of the RR has not been studied, which is the main contribution of this work. In addition, the rotational speed is an essential factor to be considered to allow for different Taylor flows and study the effects of the selected parameters under different operating conditions. The factors studied in this investigation are listed in Table 1.

4.3. Analysis setup

The ANOVA model in this study utilised factorial analysis to determine the effects of the selected factors on responses at various levels (Scheffe, 1999). This method allows for the variables to be ranked based on their influence on the objective function values (Tabatabaei et al., 2018; Larson, 2008). Therefore, parameters affecting the performance of FESS can be identified and optimised. Estimating the coefficients in a mathematical model, forecasting the response and determining the model's suitability are the main processes in the optimisation process (Eltaweel et al., 2022). To fit the proposed equations and plot response surfaces, regression analysis of the data was performed using the statistical software *Design-Expert*.

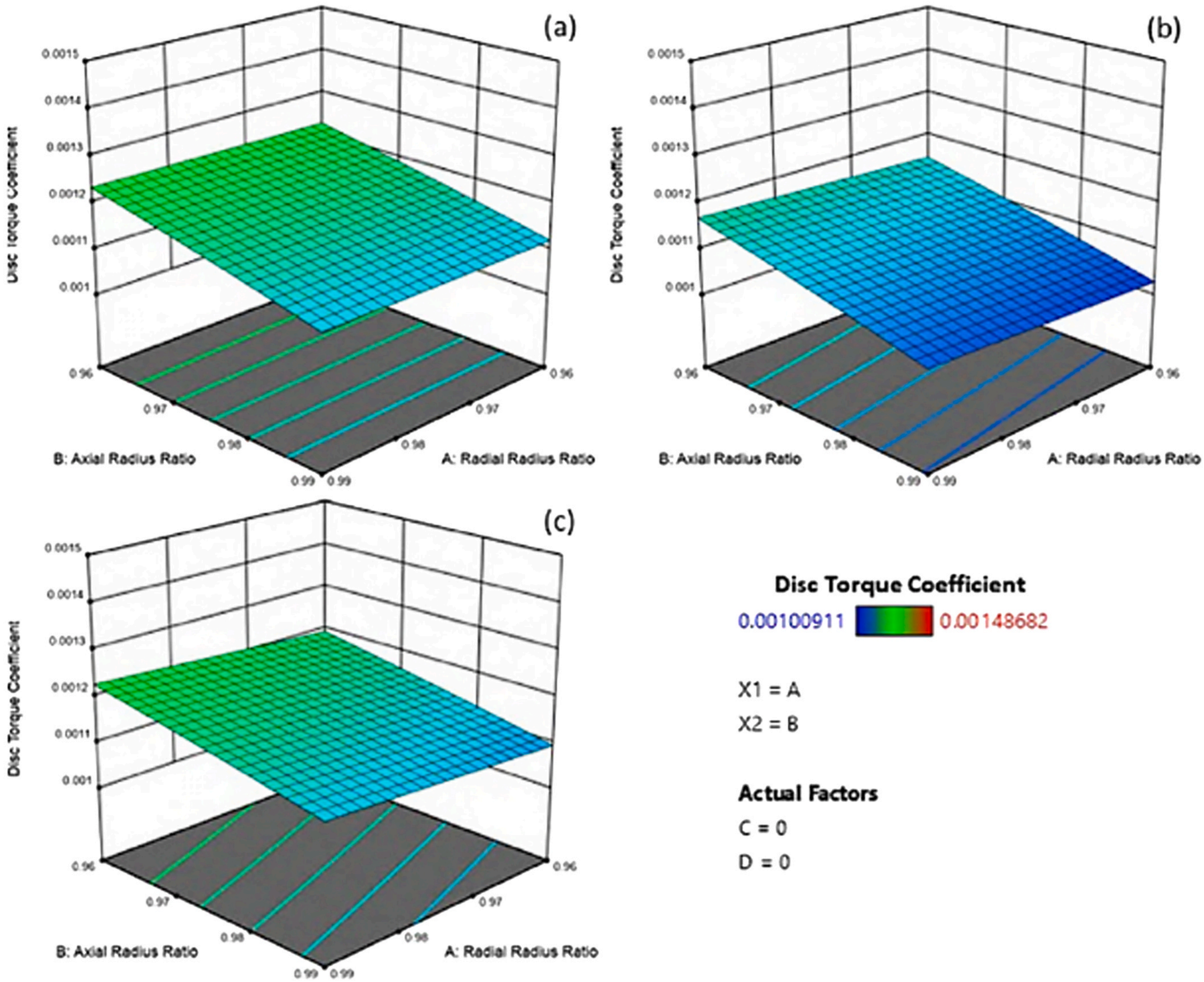

Fig. 16. 3D plot of disc torque coefficient as a function of RRR and ARR at different rotational speeds: (a) 800 rad/s, (b) 1600 rad/s, (c) 2400 rad/s.

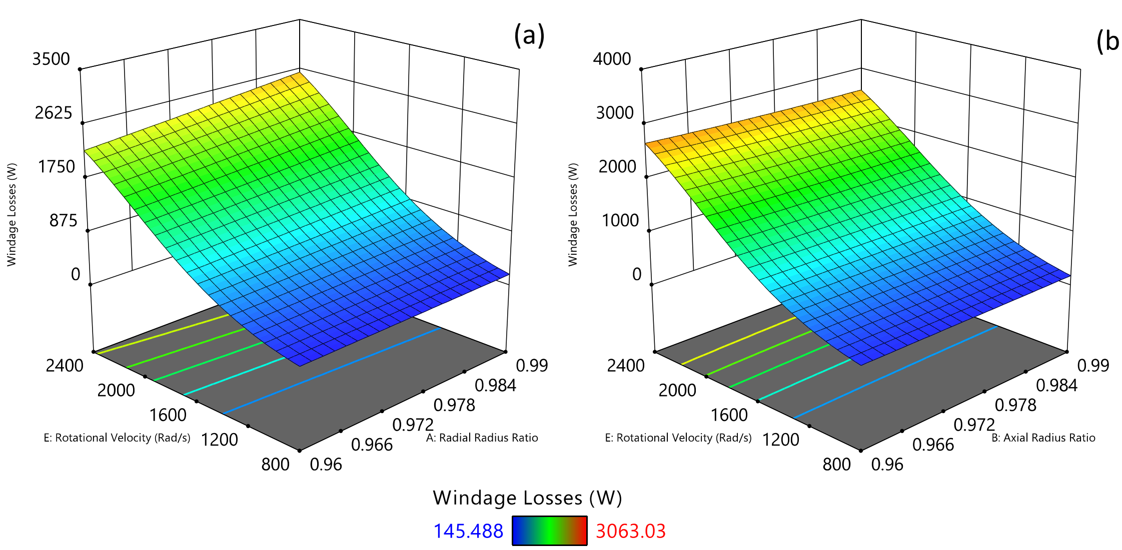

Fig. 17. 3D plot of windage losses as a function of rotational velocity and (a) RRR, (b) ARR.

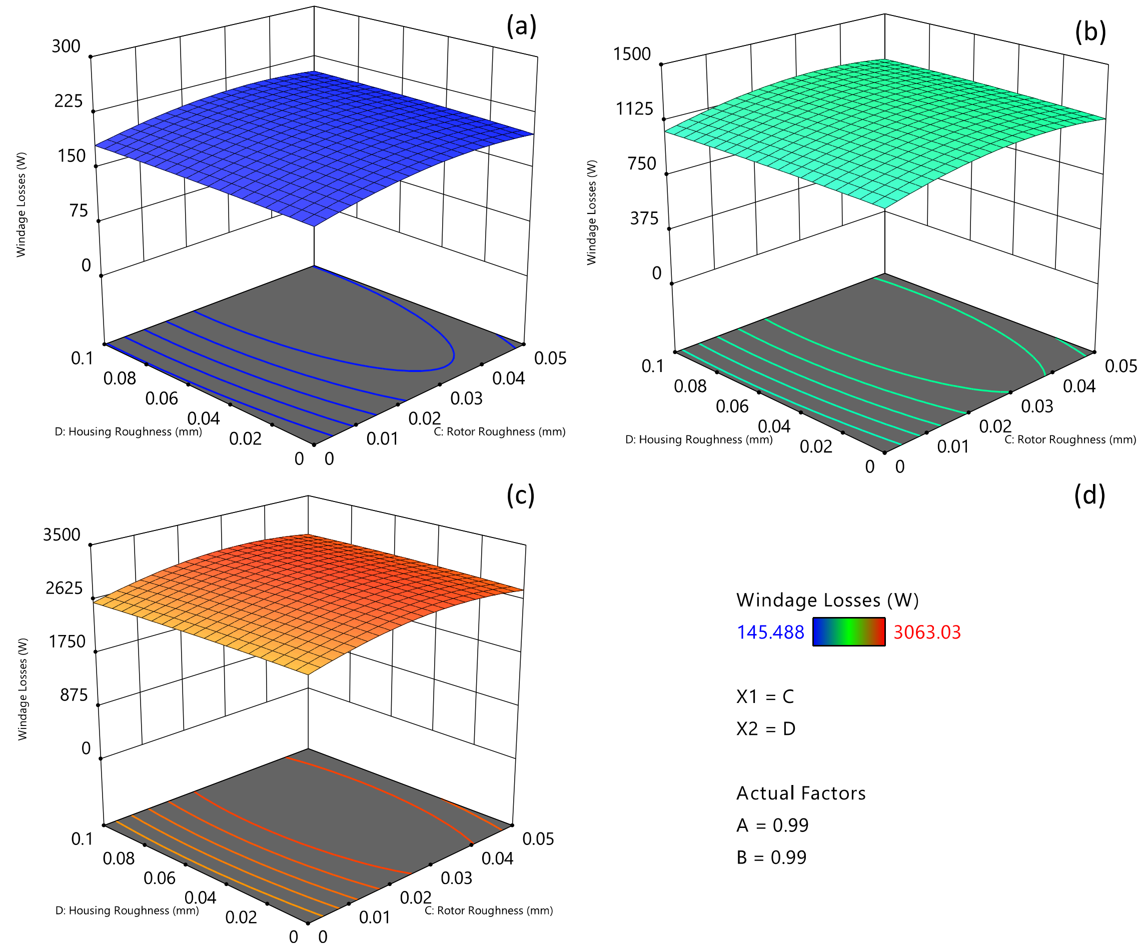

Fig. 18. 3D plot of windage losses as a function of RSR and HSR with RRR and ARR of 0.99 at different rotational speeds: (a) 800 rad/s, (b) 1600 rad/s, (c) 2400 rad/s.

5. Results and discussion

This section presents the results obtained from the parametric analysis of FESS design parameters, focusing on the effects of operating speed, airgap size, and surface roughness on windage losses and heat transfer. The findings are analysed using ANOVA to assess parameter significance and interaction effects, followed by a discussion on optimised configurations for enhanced system performance.

5.1. Influence of rotational speed

The rotor's rotational speed and the size of the airgap are the primary factors affecting the flow characteristics. The effect of rotational speed on the velocity distribution within the airgap is investigated. The FESS with different RRs has been studied at the rotational speeds of 200, 800, 1600 and 2400 rad/s. The Taylor number for all the studied cases is considerably higher than the critical Taylor number confirming the existence of Taylor vortices within the airgap. Fig. 6 depicts air velocity distribution within the airgap at the RR of 0.99; the creation of a Taylor-Couette flow in the airgap resulted in the spike-shaped flow. The air velocity near the housing wall is close to zero, while maximum velocity occurs near the rotor. It was observed that the intensity of the vortices increases as the rotational speed increases.

The airgap size determines the number of Taylor vortices, a Taylor cell is composed of two Taylor vortices which are quadrilateral in shape. Therefore, the larger the airgap size, the larger the size of the Taylor vortices, thus resulting in fewer Taylor cells within the airgap. The RRs of 0.99, 0.98, 0.97 and 0.96 resulted in Taylor cells of 48, 22, 14 and 12, respectively. As shown in Figs. 6–9, the number of Taylor cells decreases as the airgap size increases. The same effect can be seen for all the RRs investigated. As the airgap size increases, the number of Taylor cells decreases dramatically, resulting in improved heat transfer between the rotor, housing and air thus lower windage losses.

5.2. Response

The two selected responses were subjected to an analysis of variance, the results of the significant factors and their interactions are tabulated in Table 2 and Table 3 for the first response (Nusselt number) and the second response (windage loss), respectively.

The ANOVA for response surface quadratic models for Nusselt number and windage losses revealed that the models were significant, with F-values of 2431.14 and 87259.11, respectively. Model terms with P-values less than 0.05 are considered significant while model terms with values greater than 0.10 are considered insignificant. The responses shown in Table 2 and Table 3 are significant, the insignificant factors were removed to improve the model. The F-values for each factor and their interactions are calculated to determine the significance of their mean variation. The relevant P-values with a 95 % confidence interval have been calculated. Statistical results show that these models adequately predicted Nusselt number and windage losses within the range of studied variables. Table 2 and Table 3 show that each factor is significant in both responses with a P-value less than 0.05. Ensuring the adequacy of the selected model is critical to confirm that it accurately captures the underlying data patterns. Indicators of model adequacy include the normality of the data, homogeneity of variances, and the

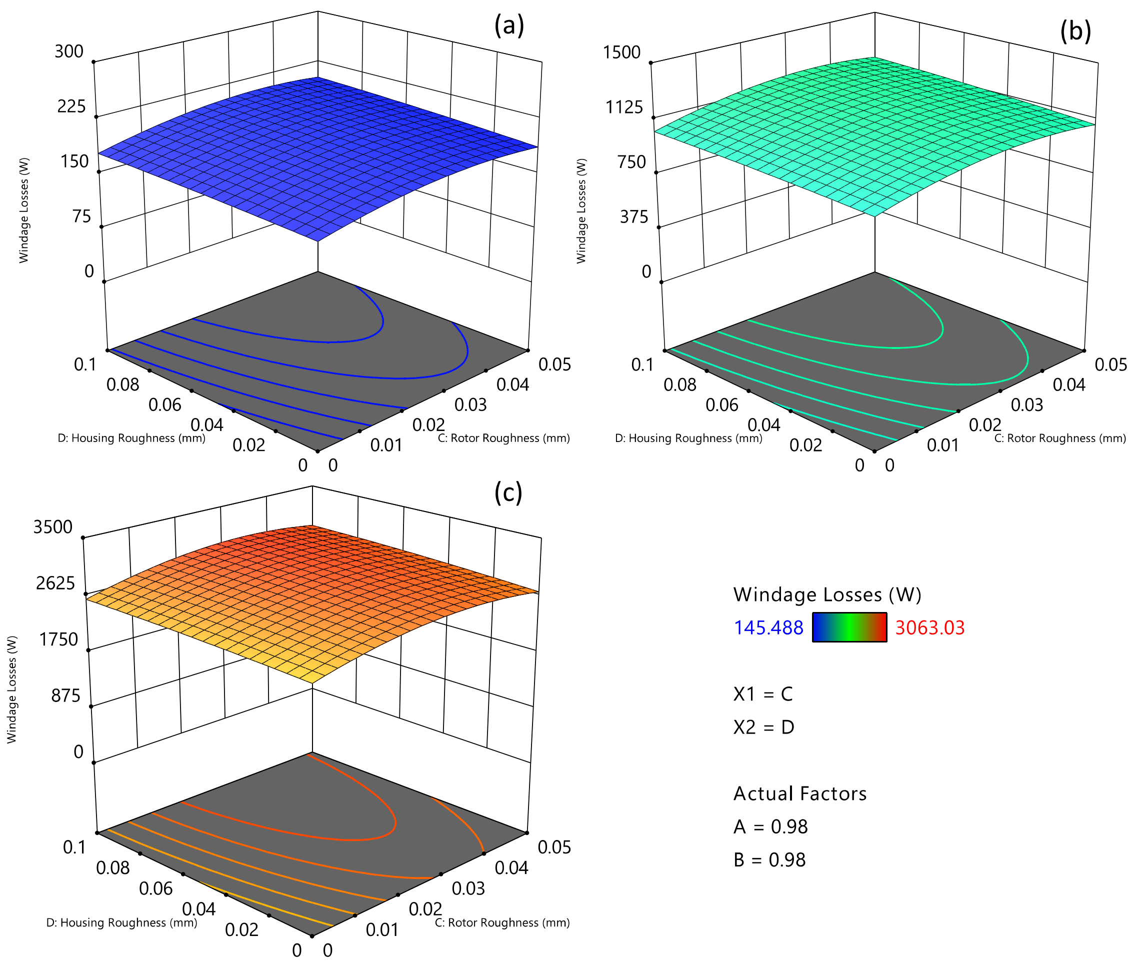

Fig. 19. 3D plot of windage losses as a function RSR and HSR with RRR and ARR of 0.98 at different rotational speeds: (a) 800 rad/s, (b) 1600 rad/s, (c) 2400 rad/s.

randomness of residuals. Initial results have shown that the model is inadequate and based on the box-cox transformation (Atkinson et al., 2021), natural log transformation for both responses was essential to resolve the lack of normality in the obtained data. After applying the transformation, further assessments were conducted to verify the improved normality, homogeneity of variances, and randomness of the data, ensuring a more reliable and accurate model fit.

The ANOVA analysis revealed that certain parameters had a more significant impact on both windage losses and Nusselt number in FESS. For windage losses, rotational velocity emerged as the most influential factor, indicating its substantial effect on drag forces. Following this, rotor surface roughness and housing surface roughness also had high F-values, underscoring their significant influence on boundary layer dynamics and frictional interactions.

When analysing the Nusselt number, which reflects the efficiency of convective heat transfer, ARR showed the highest influence, indicating that it plays a crucial role in determining heat dissipation efficiency within the system. This was followed by RRR, and rotational velocity. These results suggest that optimising airgap sizes is essential for enhancing heat transfer performance, while the effect of rotational velocity further contributes to increased convective heat transfer by promoting turbulence in the airgap.

In both cases, the surface roughness of the rotor and housing exhibited a noticeable influence, though less significant than the primary factors. For windage losses, surface roughness affects aerodynamic drag and frictional resistance. For the Nusselt number, rotor and housing roughness, contribute to enhancing heat transfer by disrupting the boundary layer, allowing for more effective heat dissipation.

5.3. Model adequacy

The mathematical model in regression analysis describes the relationship between input variables and dependent responses. Fit statistics for the initial response are shown in Table 4, indicating a high coefficient of determination (R^2) above 0.98, with minimal deviation between the regression line and response points. The adjusted R^2 values, which account for unnecessary parameters, are also above 0.98, indicating low variability. The model's ability to predict new observations is assessed using the predicted R^2, which shows a small difference of 0.2 from the adjusted R^2, indicating a good correlation. The precision ratio of 219.724 and 768.567 for the first and second responses, respectively, demonstrates sufficient signal-to-noise ratios in the data.

5.4. The Nusselt number response

The first response is the Nusselt number, an essential parameter for identifying the convective heat transfer between the rotor, air, and flywheel housing. A higher Nusselt number indicates better convection, thus lower rotor, and housing temperature within the safe range. As shown in Fig. 10, increasing the airgap size increases the Nusselt number at all rotational speeds. The highest Nusselt numbers were achieved at the RR of 0.96 in the radial and axial directions and the rotational speed of 1600 rad/s. The Nusselt number is influenced by the Reynolds number, which increases as the rotational velocity increases until it reaches 1600 rad/s, at which point it begins to fall due to reduction in the kinematic viscosity of air as the air temperature reduces further.

Taylor vortices appear more frequently as the radial airgap increases, while Taylor cells are less rapidly affected by azimuth waves as the

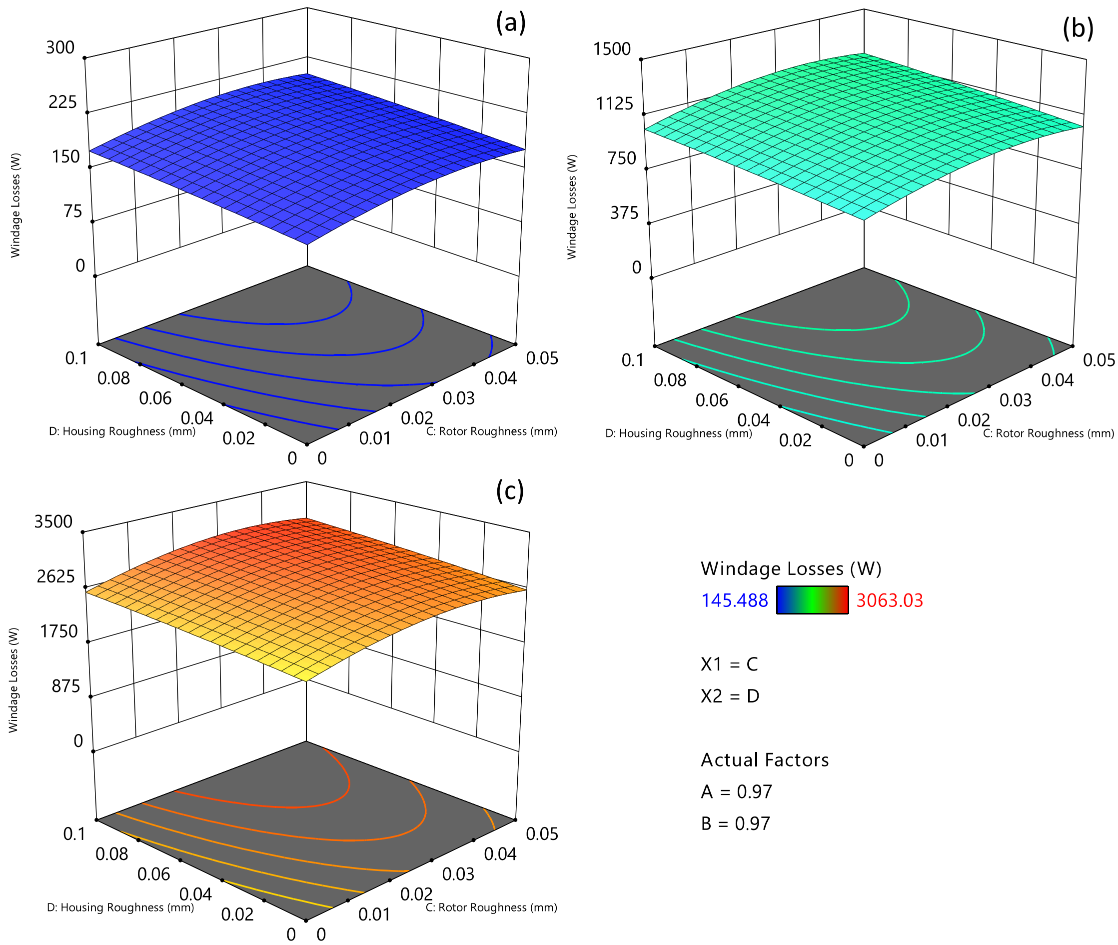

Fig. 20. 3D plot of windage losses as a function of RSR and HSR with RRR and ARR of 0.97 at different rotational speeds: (a) 800 rad/s, (b) 1600 rad/s, (c) 2400 rad/s.

radial airgap reduces (Fénot et al., 2011). As shown in Fig. 11. The increase in HSR and RSR increases the Nusselt number for all the studied rotational velocities except 2400 rad/s, where the SR did not affect the Nusselt number. The same trend was observed for the studied RRs. The Nusselt number of the roughened rotor and housing increases as the Reynolds number increases due to the increased turbulence intensity near walls. The flow regime is considered transitional between hydrodynamically smooth and fully rough when the dimensionless roughness height is between 2.25 and 90. In this case, the second and third roughness heights for the rotor and the housing are in the transitional regime.

Fig. 12a depicts the air velocity distribution within the airgap of the FESS with RRR and ARR of 0.98 at the rotational velocity of 1600 rad/s. The RSR influences the shape of the Taylor vortices and the time at which they appear. The shear applied to a rough surface is more significant than a smooth surface due to the significant decelerating force exerted on the swirling flow by the rough surface. Consequently, the rotor has the highest and the housing the lowest temperature, thus there exists a temperature gradient between the rotor and housing surfaces. The spike-shaped flow shown in Fig. 12 is due to the presence of Taylor-Couette flow in the airgap. The air velocity near the housing is close to zero, while the maximum air velocity occurs near the rotor. The air molecules at high temperatures near the rotor are moved upwards towards the housing, causing the mixing temperature to rise. This finding is explained by an increase in centrifugal forces, which increases the speed of the vortices when they collide, as shown in Fig. 12 (b) and (c).

The effect of the RRR and the rotational velocity on the Nusselt number for the studied ARRs is shown in Fig. 13. The results demonstrated that increasing the rotational velocity improves the Nusselt number until the rotational velocity of 1600 rad/s at which point, the Nusselt number begins to drop drastically. Unfortunately, manufacturers typically ignore the effect of the ARR, even though it is significant in terms of the Nusselt number, which could lead to improved heat transfer rate, higher rotational velocities and increased kinetic energy storage capacity.

5.5. *Windage loss response*

The size of the airgap, SR, rotational speed and thermo-physical properties of the confined fluid significantly affect the windage losses. The influence of the rotational speed on the windage losses is analysed for all different studied RRs. Fig. 14 depicts the windage losses for the studied rotational velocities as a function of RRRs and ARRs. Air friction is more significant in larger RRs compared to smaller RRs due to the higher shear stress produced by the Taylor vortices. The highest windage losses are achieved at the smallest airgap (i.e. highest RRs), as shown in Fig. 14. The RRR significantly affects the rotor skin friction coefficient, as shown in Fig. 15. The higher the RRR (smaller airgap), the higher the rotor skin friction coefficient. The rotor skin friction coefficient is one of the most important factors influencing windage loss since approximately 70 % of windage losses are due to frictional losses in the radial airgap while the remaining 30 % originate from the losses in the axial airgap due to disc torque. It was observed that an increase in the ARR reduced the rotor skin friction coefficient. The greater the axial distance between the rotor and the housing, the higher the heat transfer rate, resulting in lower surface temperatures. On the other hand, windage losses increase

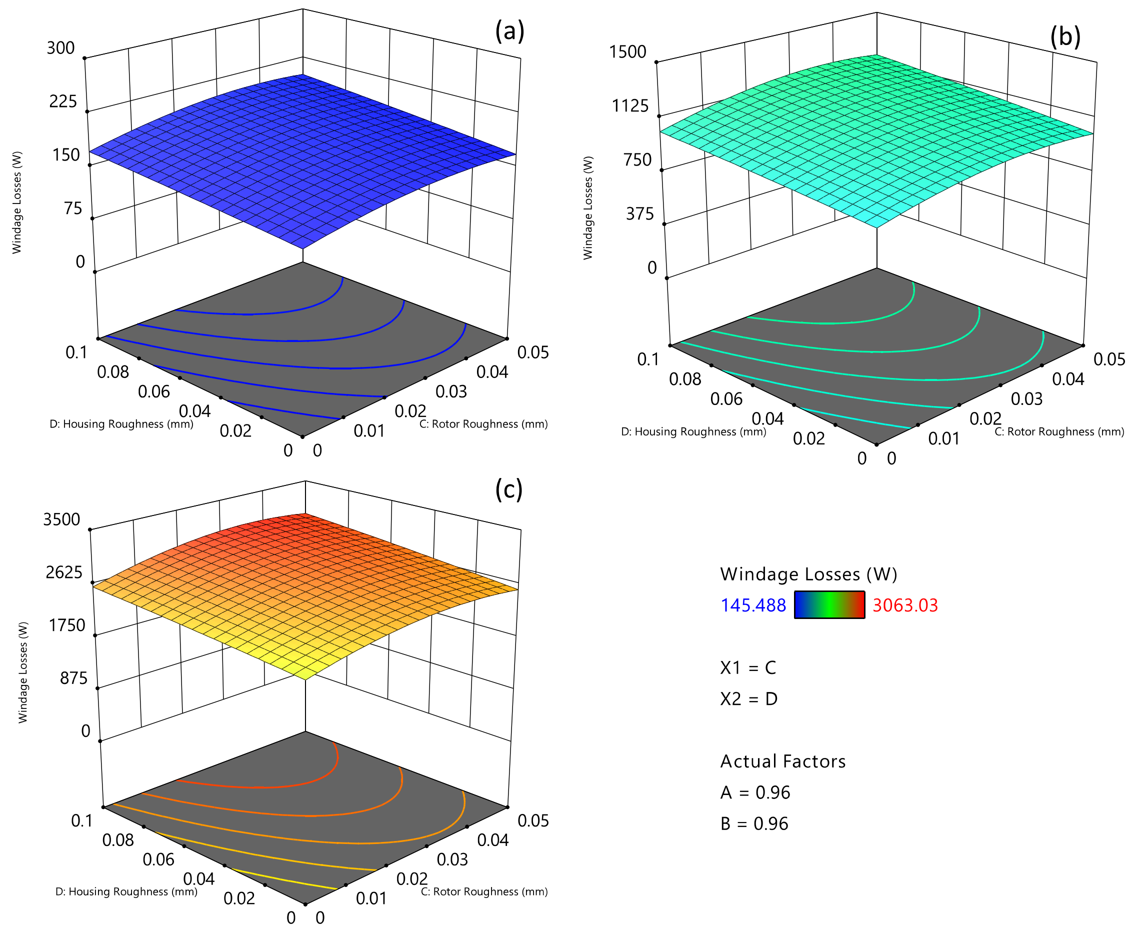

Fig. 21. 3D plot of windage losses as a function of RSR and HSR with RRR and ARR of 0.96 at different rotational speeds: (a) 800 rad/s, (b) 1600 rad/s, (c) 2400 rad/s.

slightly with increasing the axial airgap size due to the increases in the disc torque coefficient, as shown in Fig. 16. Although both *RRR and ARR* affected the disc torque coefficient, increasing the RRR slightly increased the disc torque coefficient with the lowest value occurring at 1600 rad/s.

Fig. 17. depicts the effect of rotational velocity, *RRR and ARR* on windage losses. Windage losses increase exponentially as rotational velocity increases, irrespective of the RRR or ARR. As previously stated, decreasing the RRR and increasing the ARR reduces windage losses, as shown in Fig. 17. At the maximum rotational velocity, the ARR can reduce windage losses by approximately 4 % for all the studied RRRs. In comparison, the RRR can reduce windage losses by 15 %. However, the combination of RRR of 0.99 and ARR of 0.96 can reduce windage losses by approximately 19 %.

5.6. *Influence of surface roughness*

As the Reynolds number increases, the viscous length scales in the flow decrease, and eventually, every surface appears rough even if the roughness is very small on an absolute scale (Verschoof et al., 2018). Figs. 18-21 depicts the effect of HSR and RSR on windage loss for the studied rotational velocities and RRs. The same trend is observed at each rotational velocity for all the studied RRs. The effect of HSR is small compared to the RSR. At the maximum studied rotational velocity, regardless of the RR, the difference between the lowest and highest studied HSR results in approximately 3 % increase in windage losses and a 2.7 % increase in Nusselt number. The lowest windage losses were recorded with smooth surfaces on both the rotor and the housing, indicating that SR has a negative impact on windage losses.

As shown in Figs. 18-21, the RSR significantly impacts windage losses. Windage loss increases as the RSR height increases until it reaches a peak value of 0.025 mm where it begins to decrease. The effect of RSR on windage losses is almost constant regardless of the RR, whereas the effect of HSR increases as the RR decreases. With increasing RSR, the velocity gradient close to the rotor decreases. The skin friction coefficient is a dimensionless factor, and as the Reynolds number increases, skin friction decreases until it becomes constant in the presence of SR. The absolute value of skin friction is determined based on the characteristic roughness height (Hu et al., 2022). RSR has a significant impact on the onset of Taylor vortices. The results suggest that the onset occurs at lower Reynolds numbers, while the onset of wavy Taylor vortices is more affected by the RR. Additionally, it can be concluded that the RR has a more significant impact on oscillation frequency in the wavy Taylor regime compared to SR (Pokorny et al., 2016).

The effect of SR on the rotor skin friction coefficient as a function of RRR at the maximum studied rotational velocity and a constant ARR of 0.96 is shown in Fig. 22. Compared to the effect of RSR, the effect of HSR on the skin friction coefficient is minimal. The effect of HSR is further reduced as the RRR increases. The RSR height of 0.035 mm produced the highest rotor skin friction coefficient for all the studied RRRs. The critical Taylor number at which Taylor vortices appear is significantly higher for a rotor with higher SR compared to a smooth surface. The increase in RSR postpones the emergence of the first instabilities, where the roughness height directly relates to the observed delay. The fluid particle velocity will be reduced due to the friction between the flow and the rotor; therefore, it can be deduced that the SR delays the formation

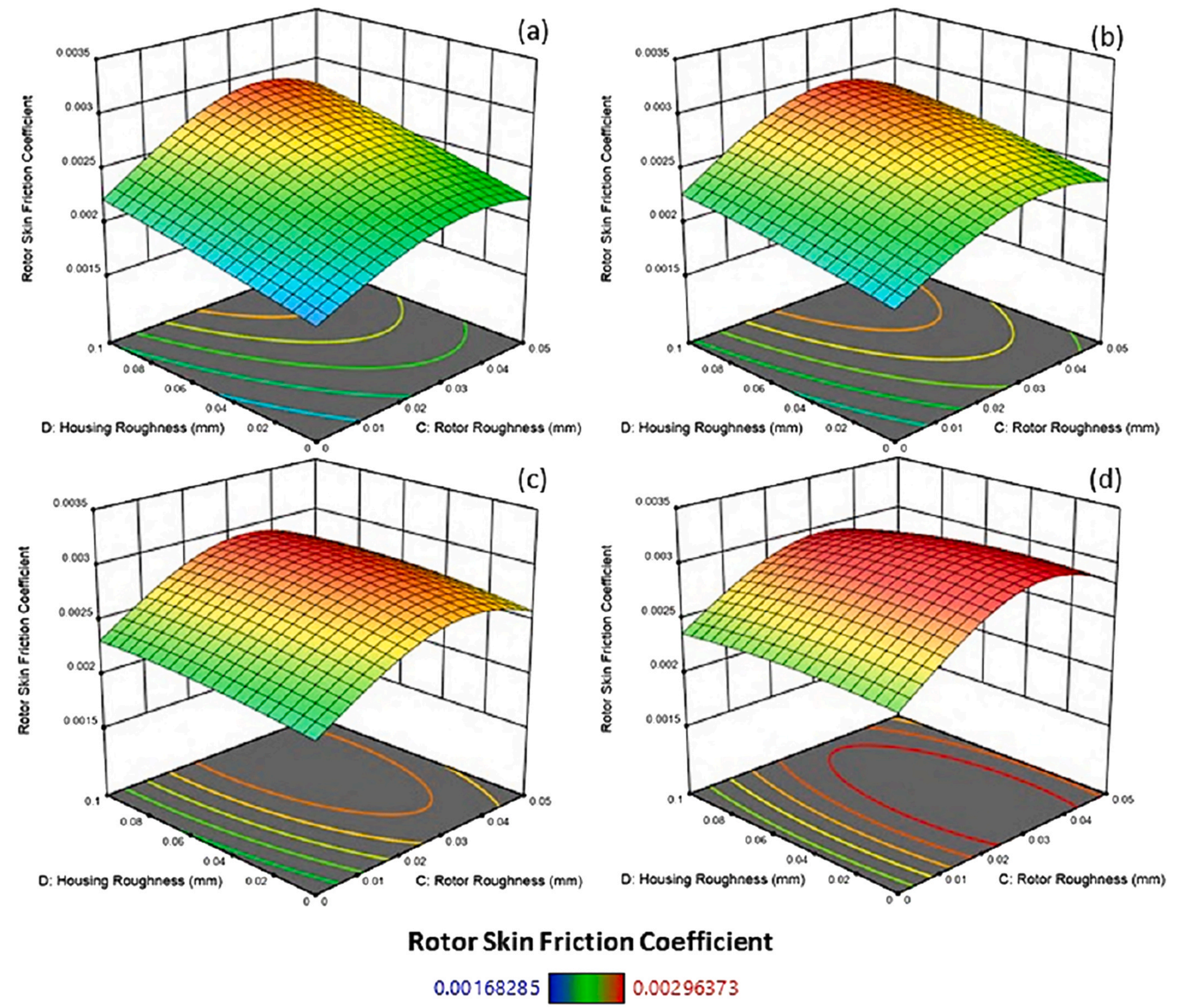

Fig. 22. 3D plot of rotor skin friction coefficient as a function of RSR and HSR at a rotational speed of 2400 rad/s with ARR of 0.96 and RRRs of: (a) 0.96, (b) 0.97, (c) 0.98, (d) 0.99.

of Taylor vortices. SR effect on Tayler cells is unnoticeable once they are present; instead, it results in flow disruption. Consequently, the transition from one flow regime to another occurs more quickly (Gaied et al., 2018). Fig. 23 depicts the effect of rotational velocity on the rotor skin friction coefficient. A similar trend is observed for the effect of RSR and HSR on disc torque coefficient as shown in Fig. 24. As the roughness height increases, the drag coefficient and the Nusselt number increase. This is explained by regions of plume ejection caused by enhanced boundary layer detachment. As a result of the strong radial velocity component present in the plumes, they significantly contribute to the Reynolds stress term of the angular velocity flux (Berghout et al., 2019).

5.7. Optimisation

The term "desirability" is used by Myers et al. (2016) to describe the multiple-response method. The desirability function, *D(X)*, is an objective function used in this method. An ideal range for each response is denoted by d_i with zero to one representing the most and the least desirable range, respectively. It is the geometric mean of all the transformed responses that constitutes the simultaneous objective function as shown in Eq. (11) (Myers et al., 2016).

$$D = (d_1 \bullet d_2 \bullet \ldots d_n)^{\frac{1}{n}} = \left(\prod_{i=1}^{n} d_i\right)^{\frac{1}{n}} \tag{11}$$

Where the number of measured responses is n. From zero outside the limits to one at the goal, desirability is an objective function. A point is found that maximises the desirability function by using numerical optimisation. Adjusting the weight or importance of a goal can change the goal's characteristics. A single desirability function is applied to a variety of responses and factors. Numerical optimisation between the system's responses was conducted using *Design-Expert* software. Given the importance of each factor, the software provided several solutions that could achieve the highest desirability, aiming at minimising the windage losses while maximising the Nusselt number. The predicted windage losses and Nusselt number for the proposed solution were compared to CFD results for each case to confirm the validity of the predicted values. The numerical and predicted values are in good agreement, with a 2 % difference for windage losses and a 4 %

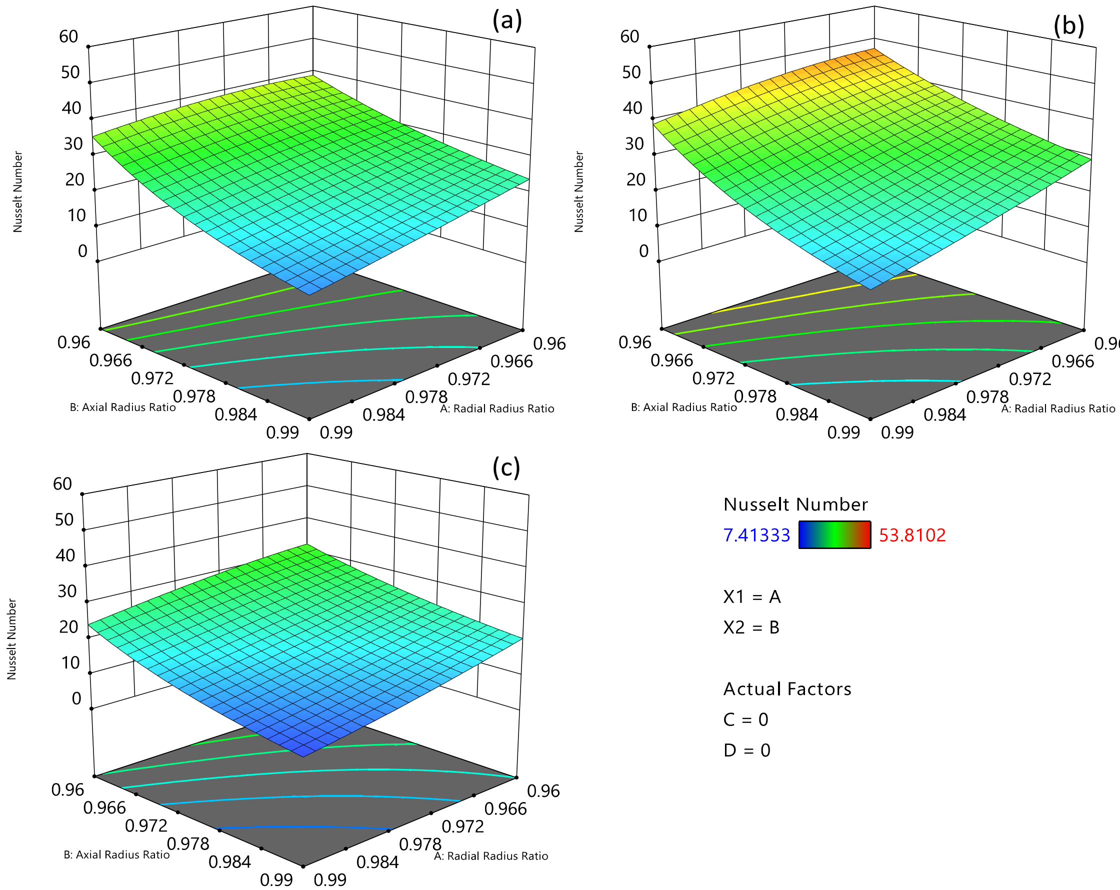

Fig. 23. 3D plot of rotor skin friction coefficient as a function of RSR and HSR at RRR and ARR of 0.96 at different rotational speeds: (a) 800 rad/s, (b) 1600 rad/s, (c) 2400 rad/s.

difference for the Nusselt number. Table 5 presents suggested solutions and their corresponding desirability values as determined by the software. Desirability levels are assigned based on the importance of reducing windage losses, ranging from one (least important) to five (most important). Increasing rotational velocity increases windage losses but also enhances kinetic energy storage capacity. Solutions one and five prioritise minimising windage losses, potentially disregarding the Nusselt number if an active cooling system is implemented. Solutions three and four are viable options when both parameters hold equal importance.

6. Discussion and implications

The findings of this study provide valuable insights into the optimisation of FESS, particularly in minimising windage losses and enhancing heat dissipation through combined parameter adjustments. By applying a comprehensive approach that examines the effects of operating speed, radial and axial airgap sizes, and surface roughness on FESS performance, this study addresses several limitations in prior research, where parameter interactions were often overlooked. The results not only demonstrate notable improvements in FESS efficiency compared to previous work but also offer practical guidance for system operators, highlighting parameter configurations that can optimise performance under varied operational conditions. This section further interprets the study's findings in comparison with existing literature, discusses practical implications for FESS deployment, and outlines key limitations of the current research to guide future studies.

Fig. 25 presents a main effects plot that explains the influence of five factors on the mean Nusselt number. It is visible from the plot that rotational velocity is a significant factor, with the Nusselt number increasing to a maximum at 1600 rad/s before the effect inverts, coinciding with a decline in the Reynolds number. Concerning the RR, a rise in the airgap, both radially and axially, is correlated with an enhancement in the Nusselt number, although the effect of ARR is found to be more pronounced. With regards to the SR, an increase in RSR is associated with an increased Nusselt number, while the impact of HSR exhibits a distinctively different trend. On the other hand, Fig. 26 presents a main effects plot that explains the influence of five factors on the mean windage losses. The plots clearly indicate that an increase in rotational velocity results in a substantial increase in windage losses. In contrast, a reduction in the RRR contributes to a decrease in windage losses, an effect that is inversely observed with the ARR where its reduction leads to increased losses. Furthermore, the complete removal of SF is shown to contribute to a reduction in windage losses, irrespective of whether the SF are on the rotor or the housing.

The optimisation of FESS design parameters in this study has led to significant improvements in both windage loss reduction and heat transfer efficiency. The optimal configuration at the highest rotational velocity was found to involve a radial radius ratio of 0.96 and an axial radius ratio of 0.97, with a rotor surface roughness of 1.9e-7 m and a housing surface roughness of 6.9e-7 m. This setup effectively balances enhanced heat transfer with minimal windage losses.

The results indicate that increasing the radial airgap size reduces windage losses and enhances the Nusselt number, while increasing the axial airgap size raises both windage losses and heat transfer. As the airgap size increases, the number of Taylor cells decreases, facilitating better heat transfer between the rotor, air, and housing and contributing to reduced windage losses. For all radial radius ratios studied, an increase in axial radius ratio reduced windage losses by approximately 4 % at maximum rotational velocity, while the radial radius ratio alone

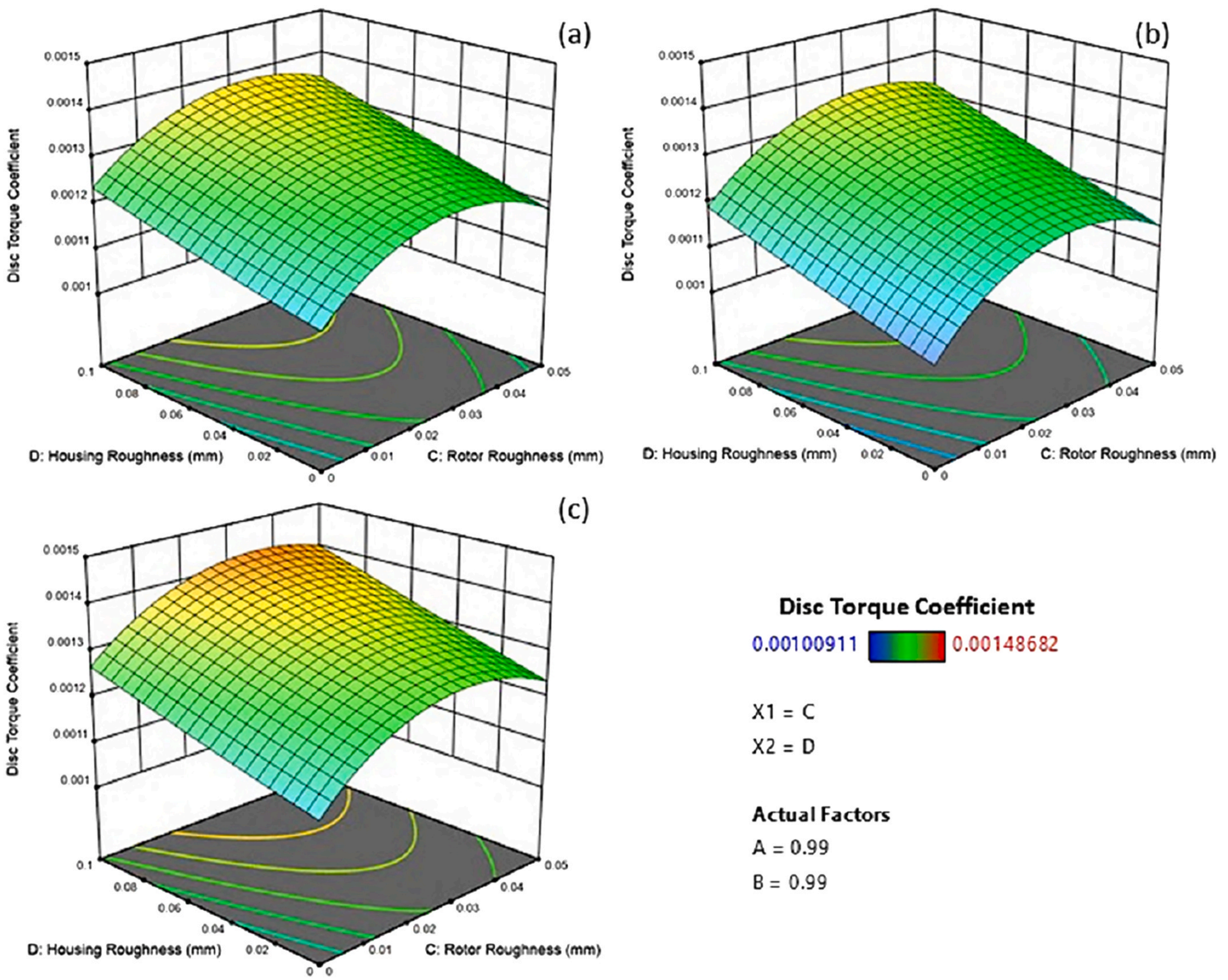

Fig. 24. 3D plot of disc torque coefficient as a function of RSR and HSR at RRR and ARR of 0.99 at different rotational speeds: (a) 800 rad/s, (b) 1600 rad/s, (c) 2400 rad/s.

Table 5
The desirability levels for the suggested solutions.

#	Importance values	RRR	ARR	RSR (m)	HSR (m)	Rotational Velocity (ω) (rad/s)	Predicted Windage Losses (WL) (Watt)	CFD Windage Losses (Watt)	Predicted Nusselt Number (Nu)	CFD Nusselt Number	Desirability
1	WL= 5 Nu= 1	0.96	0.962	6.7e−8	2.2e−5	1944	1478	1505	41.56	43.28	0.836
2	WL= 1 Nu= 5	0.96	0.96	7.5e−5	7.5e−6	2291	2098	2121	35.25	34.47	0.661
3	WL= 3 Nu= 3	0.96	0.96	1.4e−7	4.8e−7	2060	1695	1685	40.67	41.68	0.458
4	WL= 5 Nu= 5	0.96	0.96	4.6e−7	6.9e−7	1911	1423	1424	43.61	45.35	0.453
5	WL= 5 Nu= 1	0.96	0.97	1.9e−7	6.9e−7	2400*	2230	2259	26.80	26.26	0.371

* Maximum velocity is fixed to achieve the maximum storage capacity.

contributed to a 15 % reduction.

Surface roughness plays a nuanced role; both the rotor and housing roughness increase windage losses but simultaneously improve the Nusselt number. At the maximum rotational velocity, regardless of radius ratio, the housing surface roughness was observed to increase windage loss by approximately 3 % and enhance the Nusselt number by 2.7 %.

6.1. *The effects of taylor-couette flow on system performance*

Taylor-Couette flow, characterised by the formation of Taylor vortices, plays a significant role in influencing windage loss and heat

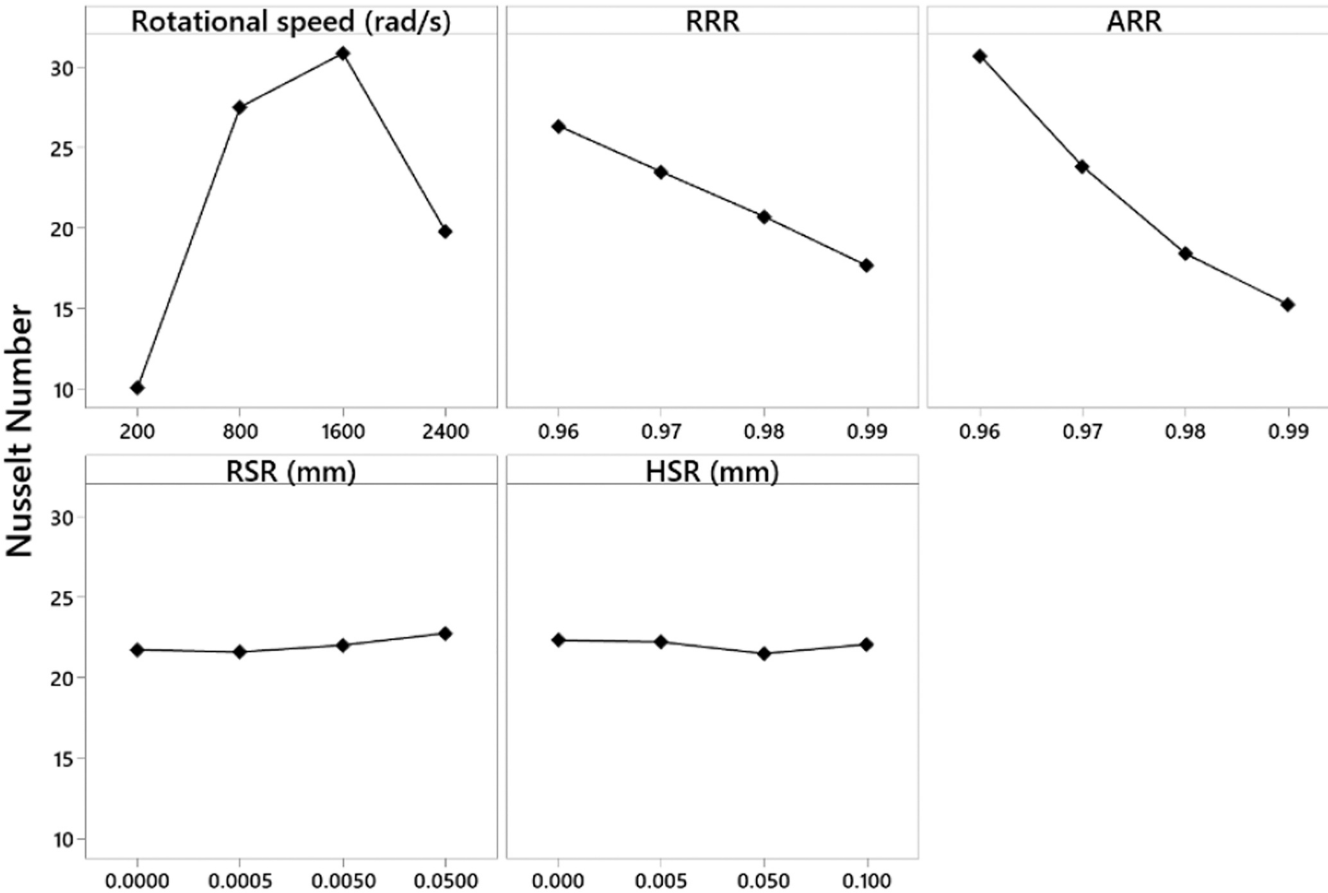

Fig. 25. Main effects plot for mean Nusselt number for the studied five factors.

transfer in FESS. Specific operating conditions and design choices can indeed be optimised to either enhance or mitigate these effects, depending on the desired performance outcomes. Increasing the rotational speed is one way to intensify Taylor vortex formation, which could enhance convective heat transfer within the system. However, this also increases windage losses, creating a trade-off between improved heat dissipation and energy efficiency. Adjusting the radial airgap size also impacts Taylor-Couette flow behaviour, as narrower airgaps can lead to stronger vortex formation, which can be beneficial for heat transfer but will again increase drag forces and windage losses. Further, altering the design of the housing interior, such as by introducing slits or other structural modifications, can influence the development and behaviour of Taylor-Couette flow. Adding slits within the housing can disrupt the vortices or modify their pattern, thereby providing additional control over both heat transfer and windage losses. This design adjustment could allow for more effective heat dissipation while minimising the drag forces associated with vortex formation.

Design choices that could help balance these effects include optimising the rotor surface roughness to control boundary layer interactions and tailoring the airgap dimensions to moderate vortex formation. For instance, a carefully selected roughness on the rotor surface could influence the onset and intensity of Taylor vortices, thereby controlling heat transfer without excessively increasing drag. Additionally, selecting optimal airgap sizes to maintain Taylor-Couette flow within transitional flow regimes could allow for effective heat transfer while limiting the intensity of vortices, helping to reduce windage losses.

6.2. Advancements over previous studies

This study represents a significant advancement in the optimisation of FESS by focusing on passive design improvements rather than introducing additional complexities, such as partial vacuums or active cooling systems. By optimising surface roughness, airgap size, and operating speed, this research achieves substantial gains in performance without the need for energy-intensive auxiliary components.

Previous studies have highlighted the benefits of specific design parameters but often relied on complex setups or additional systems. Table 6 summarizes key findings from these studies and how the present work expands upon them through an integrated, passive optimisation approach.

These findings underscore the substantial impact of passive optimisation strategies on FESS performance. For instance, Walton et al. (2012) demonstrated that rotor-stator gap optimisation can reduce windage losses; however, their work relied on controlled ambient pressures. By contrast, this study achieves a balanced reduction in windage losses and thermal efficiency improvements without requiring controlled conditions.

In the work of Okada et al (Okada et al., 2017)., shrouding the rotor was shown to reduce windage loss while preserving motor efficiency. Here, the current study achieves comparable results through careful roughness and airgap optimisation, maintaining simplicity in design by avoiding structural modifications like shrouding. Furthermore, the findings of Tachibana and Fukui, (1964) and Howey et al. (2010) underscore the importance of airgap dimensions in controlling heat dissipation and drag. This study integrates these insights by balancing airgap size and surface roughness to optimise both thermal dissipation and windage reduction.

6.3. Practical insights for operators

This study offers practical insights for operators aiming to maximise

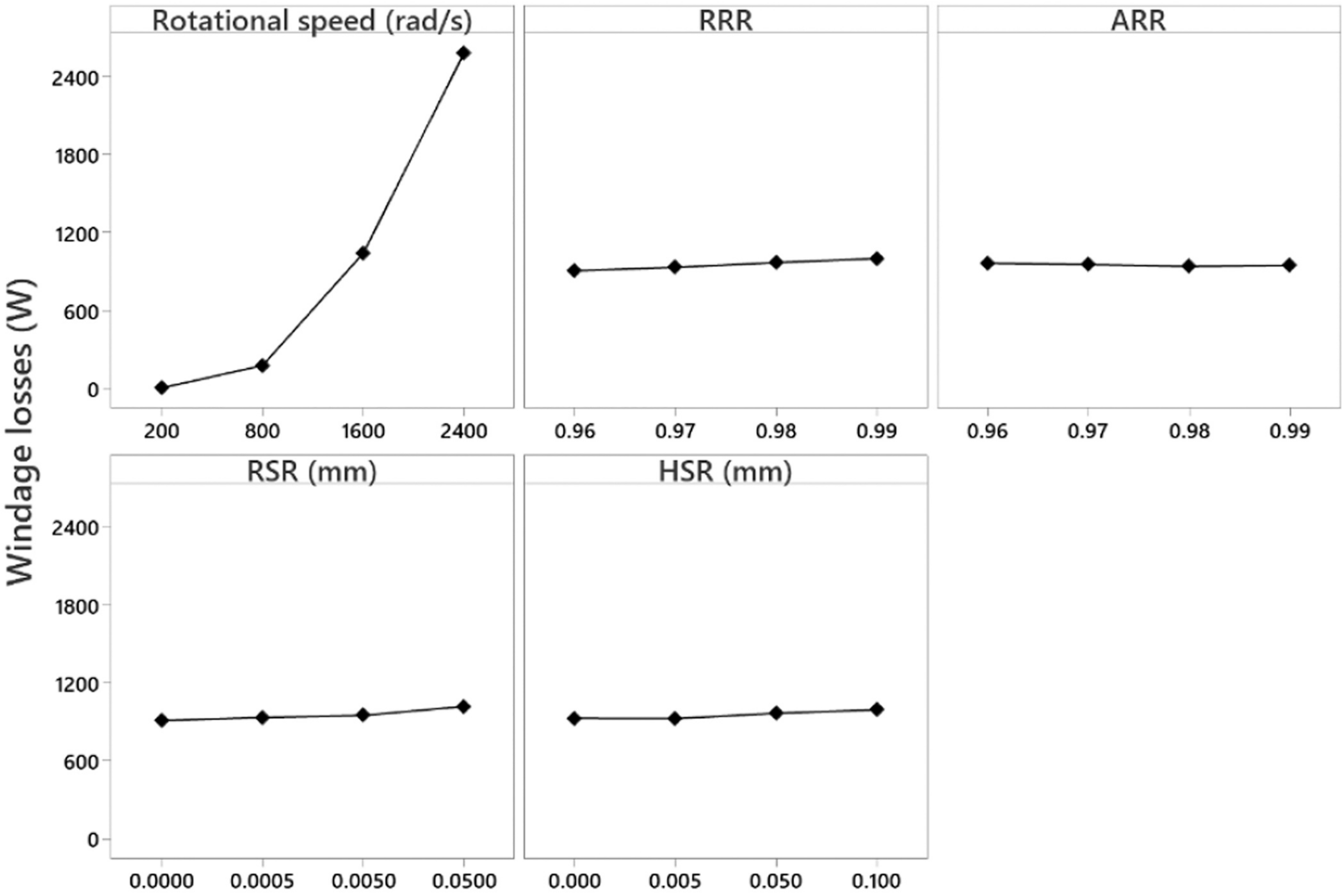

Fig. 26. Main effects plot for mean windage losses for the studied five factors.

Table 6
Comparison of key findings in previous studies and advancements in the current study.

Study	Focus	Key Findings	Advancement in Current Study
Walton et al (Walton et al., 2012).	Experimental power loss reduction in high-speed micro-turbomachinery	Demonstrated that optimising rotor-stator gaps reduces windage losses	Combines multi-parameter approach, optimising both thermal efficiency and drag
Hu et al (Hu et al., 2024).	Impact of rotor roughness on heat transfer in rotor-stator cavities	Found roughness significantly affects heat transfer and pressure distribution	Achieves passive thermal management through optimised roughness
Okada et al (Okada et al., 2017).	Shrouded rotor design to reduce windage loss in hybrid motors	Showed shrouding could decrease windage while preserving efficiency	Utilises surface roughness optimisation to achieve a similar effect without shrouding
Tachibana et al (Tachibana and Fukui, 1964).	Effect of airgap size on heat generation and dissipation in electric motors	Established sensitivity of heat generation to airgap size	Focuses on airgap optimisation in both radial and axial direction to balance heat dissipation and drag
Howey et al (Howey et al., 2010).	Airgap impact on convective heat transfer in electric motors	Highlighted airgap's effect on convective transfer in swirling air flows	Integrates airgap adjustments with optimised roughness to improve thermal control

FESS efficiency through passive optimisation. Adjusting rotor speed and airgap size can effectively balance windage losses and heat dissipation. Operators can reduce drag by carefully controlling rotational velocity while increasing the radial airgap size minimizes windage losses and enhances heat transfer. However, a larger axial airgap size can increase windage losses, so balancing radial and axial airgaps is essential to manage Taylor–Couette flow effects efficiently.

Surface roughness adjustments also provide a practical method for enhancing heat dissipation. Increased surface roughness on both rotor and housing can improve the Nusselt number, allowing for better thermal management. By selecting materials with optimal roughness characteristics, such as steel for rotors and aluminium for housing, operators can achieve effective heat dissipation with minimal impact on windage losses. These adjustments offer a straightforward approach for enhancing FESS performance without relying on complex cooling or vacuum systems, supporting more sustainable and adaptable energy storage solutions.

6.4. Scalability and broader applicability

The optimised designs presented in this study are intended to be scalable and adaptable across various sizes and applications of FESS. Key parameters, such as radius ratio and surface roughness, were specifically chosen to ensure that the optimisation principles developed here would be relevant for both small- and large-scale FESS. The use of dimensionless parameters, such as the radius ratio, allows these findings to be applied consistently across different scales without compromising the fundamental relationships between design variables and performance. While the CFD modelling used in this study has inherent computational limits, the optimisation strategies remain valid for larger FESS applications, supporting scalability in a variety of contexts.

While this study is geared toward transport decarbonisation, the optimisation strategies can be adapted to other sectors, including renewable energy storage and industrial machinery. The core design principles, such as optimising surface roughness, airgap size, and rotational speed to reduce windage losses and enhance heat transfer, are broadly applicable across applications. Scaling would primarily involve adjusting the system size to match energy storage demands.

The emphasis on radius ratio in this study supports scalability, as it provides a basis for flexible FESS designs across different capacities. This adaptability underlines the broader relevance of the study's findings, which can be leveraged for a range of energy storage and efficiency applications beyond transport, offering sustainable and high-efficiency solutions across multiple sectors.

6.5. Limitations

This study incorporates certain simplifications within the CFD model to focus on the primary factors affecting windage losses and heat transfer in FESS. Assumptions, such as neglecting gravitational effects and treating air as an ideal gas, were made to streamline the computational analysis. These assumptions are justified under typical FESS operating conditions, where the influence of rotational forces outweighs gravitational effects, rendering gravity negligible in the context of rotor dynamics and aerodynamic drag. Additionally, the ideal gas assumption holds within the standard temperature and pressure ranges encountered in FESS, as deviations from ideal gas behaviour are minimal.

However, under extreme conditions—such as very high rotational speeds or elevated pressures—non-ideal gas behaviour may become more significant. Incorporating these effects could enhance model accuracy under such conditions but would also increase computational complexity. Consequently, while these assumptions allow for an efficient analysis of the primary optimisation parameters, they may restrict the model's accuracy outside the studied parameter levels.

7. Conclusion and future work

In this study, ANOVA method and comprehensive CFD simulations were used to optimise the main geometrical and operating parameters affecting flywheel energy storage performance. To determine the validity of the CFD results, model validation was performed, which revealed a good agreement between the numerical and experimental data. The results showed that increasing the radial airgap size reduces windage losses and increases the Nusselt number while increasing the axial airgap size increases the windage losses and the Nusselt number. The number of Taylor cells decreases as the airgap size increases, resulting in improved heat transfer between the rotor, air and housing, thus lower windage losses. For all the studied radial radius ratios, the axial radius ratio could reduce the windage losses by approximately 4 % at the maximum rotational velocity. In comparison, the radial radius ratio could reduce the windage losses by 15 % and the rotor and housing surface roughness increase the windage losses while improving the Nusselt number. At the maximum rotational velocity studied, regardless of the radius ratio, the housing surface roughness can increase the windage loss by approximately 3 % and the Nusselt number by 2.7 %. Several optimal values for the investigated parameters were determined based on the importance of windage losses and heat transfer rate. ANOVA optimisation was performed, with numerical values in good agreement with the model predictions. The sensitivity of the results to variations in surface roughness was evaluated by examining different roughness heights that allowed for comparison across smooth and transitional systems. This approach provides insights into how changes in roughness impact windage losses and heat transfer, especially when considered in combination with other parameters like radial airgap size. The chosen CFD-ANOVA approach within DOE offered both computational efficiency and the level of interaction detail required for this study's objectives, providing an optimal balance for understanding and optimising FESS performance. The critical contribution of this work is studying the relationships and effects of various parameters on the performance of flywheel energy storage, which can pave the way for the implementation of energy-efficient flywheel energy storage systems for transport decarbonisation. Future work can be directed to explore the integration of active cooling as a complementary strategy alongside the passive optimisation methods addressed in this work. Another future direction can build upon the optimised FESS parameters developed in this study which demonstrates strong potential for energy recovery applications, offering certain advantages over systems like regenerative braking and ultra-capacitors in specific contexts.

CRediT authorship contribution statement

Mohammad Reza Herfatmanesh: Writing – review & editing, Validation, Supervision, Funding acquisition, Conceptualization. **Yong Chen:** Writing – review & editing, Supervision. **Mahmoud Eltaweel:** Writing – original draft, Visualization, Validation, Methodology, Investigation, Formal analysis, Conceptualization. **Christos Kalyvas:** Supervision. **Noha A. Mostafa:** Writing – review & editing, Writing – original draft, Validation, Methodology.

Declaration of Competing Interest

The authors declare that they have no known competing financial interests or personal relationships that could have appeared to influence the work reported in this paper.

Acknowledgements

This work is supported by the European Union's Horizon 2020 research and innovation programme under the Marie Skłodowska-Curie grant agreement No 801604.

Data availability

Data will be made available on request.

References

'Energy Technology Perspectives 2020 – Analysis', IEA. Accessed: Oct. 06, 2022. [Online]. Available: ⟨https://www.iea.org/reports/energy-technology-perspectives-2020⟩.

Abbas, A.T., Al-Abduljabbar, A.A., Alnaser, I.A., Aly, M.F., Abdelgaliel, I.H., Elkaseer, A., 2022. A closer look at precision hard turning of AISI4340: multi-objective optimization for simultaneous low surface roughness and high productivity. Materials 15 (6), 2106.

Amiryar, M.E., Pullen, K.R., 2020. Analysis of standby losses and charging cycles in flywheel energy storage systems. Energies 13 (17), 4441.

Anderson, K.R., Lin, J., McNamara, C., Magri, V., 2015. CFD study of forced air cooling and windage losses in a high speed electric motor. J. Electron. Cool. Therm. Control 5 (02), 27.

Anderson, J.D., Wendt, J., 1995. Computational fluid dynamics, 206. Springer.

Andersson, B., Andersson, R., Håkansson, L., Mortensen, M., Sudiyo, R., Van Wachem, B., 2011. Computational fluid dynamics for engineers. Cambridge university press.

Aoki, H., Nohira, H., Arai, H., 1967. Convective heat transfer in an annulus with an inner rotating cylinder. Bull. JSME 10 (39), 523–532.

A.C. Atkinson, M. Riani, and A. Corbellini, 'The box–cox transformation: Review and extensions', 2021.

M. Awad and W. Martin, 'Windage loss reduction study for TFTR pulse generator', presented at the 17th IEEE/NPSS Symposium Fusion Engineering (Cat. No. 97CH36131), IEEE, 1997, pp. 1125–1128.

Aydogmus, O., Boztas, G., Celikel, R., 2022. Design and analysis of a flywheel energy storage system fed by matrix converter as a dynamic voltage restorer. Energy 238, 121687. https://doi.org/10.1016/j.energy.2021.121687.

Bamisile, O., Zheng, Z., Adun, H., Cai, D., Ting, N., Huang, Q., Oct. 2023. Development and prospect of flywheel energy storage technology: a citespace-based visual analysis. 2022 3rd Int. Conf. Power Electr. Eng. 9, 494–505. https://doi.org/10.1016/j.egyr.2023.05.147.

Berghout, P., Zhu, X., Chung, D., Verzicco, R., Stevens, R.J., Lohse, D., 2019. Direct numerical simulations of taylor–couette turbulence: the effects of sand grain roughness. J. Fluid Mech. 873, 260–286.

Childs, P.R., 2010. Rotating flow. Elsevier.

Chiriță, I., Tănase, N., Apostol, S.E., Ilie, C., Popa, M., 2017. Design optimization of a flywheel using solidworks modeling and simulation capabilities'. presented at the 2017 International Conference on ENERGY and ENVIRONMENT (CIEM). IEEE, pp. 344–348.
Choudhary, S., Ninawe, A., Bawane, S., 2012. Design and optimization of flywheel—a past review'. Gold. Res. Thoughts 1 (12), 1–3.
Donnelly, R., 1958. Experiments on the stability of viscous flow between rotating cylinders I. Torque measurements. Proc. R. Soc. Lond. Ser. Math. Phys. Sci. 246 (1246), 312–325.
Donnelly, R., Simon, N., 1960. An empirical torque relation for supercritical flow between rotating cylinders. J. Fluid Mech. 7 (3), 401–418.
Doucette, R.T., McCulloch, M.D., Feb. 2011. A comparison of high-speed flywheels, batteries, and ultracapacitors on the bases of cost and fuel economy as the energy storage system in a fuel cell based hybrid electric vehicle. J. Power Sources 196 (3), 1163–1170. https://doi.org/10.1016/j.jpowsour.2010.08.100.
Eltaweel, M., et al., Nov. 2022. Application of the ANOVA method in the optimization of a thermoelectric cooler-based dehumidification system. Energy Rep. 8, 10533–10545. https://doi.org/10.1016/j.egyr.2022.08.193.
Eltaweel, M., Herfatmanesh, M.R., 2023a. Numerical Investigation of Windage Loss and Heat Transfer in a High-Speed Flywheel Energy Storage System With Slit Wall'. presented at the Turbo Expo: Power for Land, Sea, and Air. American Society of Mechanical Engineers. V006T09A013.
M. Eltaweel and M.R. Herfatmanesh, 'Analysis of Standby Power in an Enclosed High-Speed Flywheel Energy Storage System Using the CFD-ANOVA Approach', SAE Technical Paper, 2023b.
Erhan, K., Özdemir, E., 2021. Prototype production and comparative analysis of high-speed flywheel energy storage systems during regenerative braking in hybrid and electric vehicles. J. Energy Storage 43, 103237.
Fénot, M., Bertin, Y., Dorignac, E., Lalizel, G., 2011. A review of heat transfer between concentric rotating cylinders with or without axial flow. Int. J. Therm. Sci. 50 (7), 1138–1155.
L. Gaied, E. Berrich, M. Bigerelle, and F. Aloui, 'Experimental study of the wall surfaces' roughness influence on the hydrodynamics' instabilities in a Couette-Taylor flow', presented at the 23èmeCongrès Français de Mécanique, 2018.
Genta, G., . Butterworth-Heinemann, 1985.Kinetic energy storage: theory and practice of advanced flywheel systems.
Han, Y., Ren, Z., Tong, Y., Jan. 2012. General design method of flywheel rotor for energy storage system. 2012 Int. Conf. Future Energy Environ. Mater. 16, 359–364. https://doi.org/10.1016/j.egypro.2012.01.059.
Hosain, M.L., Fdhila, R.B., Rönnberg, K., 2017. Taylor-couette flow and transient heat transfer inside the annulus air-gap of rotating electrical machines. Appl. Energy 207, 624–633.
Howey, D.A., Childs, P.R., Holmes, A.S., 2010. Air-gap convection in rotating electrical machines'. IEEE Trans. Ind. Electron. 59 (3), 1367–1375.
Howey, D.A., Holmes, A.S., Pullen, K.R., 2011. Measurement and CFD prediction of heat transfer in air-cooled disc-type electrical machines'. IEEE Trans. Ind. Appl. 47 (4), 1716–1723.
Hu, L., Deng, Q., Liu, Z., Li, J., Feng, Z., 2022. Effects of surface roughness on windage loss and flow characteristics in shaft-type gap with critical CO2. Appl. Sci. 12 (24), 12631.
Hu, B., Yao, Y., Wang, C., Chen, X., 2024. The effect of rotor roughness on flow and heat transfer in rotor–stator cavities with different axial gap'. Appl. Therm. Eng., 123535
Jia, Y., Wu, Z., Bao, M., Zhang, J., Yang, P., Zhang, Z., Nov. 2022. Control strategy of MW flywheel energy storage system based on a six-phase permanent magnet synchronous motor. Energy Rep. 8, 11927–11937. https://doi.org/10.1016/j.egyr.2022.09.048.
Jungreuthmayer, C., et al., 2011. A detailed heat and fluid flow analysis of an internal permanent magnet synchronous machine by means of computational fluid dynamics'. IEEE Trans. Ind. Electron. 59 (12), 4568–4578.
Kadivar, M., Tormey, D., McGranaghan, G., May 2021. A review on turbulent flow over rough surfaces: fundamentals and theories. Int. J. Thermofluids 10, 100077. https://doi.org/10.1016/j.ijft.2021.100077.
Kale, V., Secanell, M., 2018. A comparative study between optimal metal and composite rotors for flywheel energy storage systems. Energy Rep. 4, 576–585.
Kim, C., Lee, K.-S., Yook, S.-J., 2016. Effect of air-gap fans on cooling of windings in a large-capacity, high-speed induction motor. Appl. Therm. Eng. 100, 658–667.
Larson, M.G., 2008. Analysis of variance. Circulation 117 (1), 115–121.
Li, X., Mittelstedt, C., Binder, A., 2022. A review of critical issues in the design of lightweight flywheel rotors with composite materials'. E Elektro Inf. 139 (2), 204–221.
Li, X., Palazzolo, A., 2022. A review of flywheel energy storage systems: state of the art and opportunities'. J. Energy Storage 46, 103576.
Liu, H.-P., Werst, M., Hahne, J.J., Bogard, D., 2003. Prediction of windage losses of an enclosed high speed composite rotor in low air pressure environments', presented at. Heat. Transf. Summer Conf. 15–23.
Lukic, S.M., Cao, J., Bansal, R.C., Rodriguez, F., Emadi, A., 2008. Energy storage systems for automotive applications. IEEE Trans. Ind. Electron. 55 (6), 2258–2267.
Lv, C., Zhang, J., Li, Y., Yuan, Y., Mar. 2015. Mechanism analysis and evaluation methodology of regenerative braking contribution to energy efficiency improvement of electrified vehicles. Energy Convers. Manag. 92, 469–482. https://doi.org/10.1016/j.enconman.2014.12.092.
Mehraban, A., Farjah, E., Ghanbari, T., Garbuio, L., 2023a. Integrated optimal energy management and sizing of hybrid battery/flywheel energy storage for electric vehicles. IEEE Trans. Ind. Inform.
Mehraban, A., Ghanbari, T., Farjah, E., 2023b. AI-based control of storage capacity in high power density energy storage systems, used in electric vehicles. IEEE Trans. Transp. Electrification.
Motaman, S., Eltaweel, M., Herfatmanesh, M.R., Knichel, T., Deakin, A., May 2023. Numerical analysis of a flywheel energy storage system for low carbon powertrain applications. J. Energy Storage 61, 106808. https://doi.org/10.1016/j.est.2023.106808.
Myers, R.H., Montgomery, D.C., Anderson-Cook, C.M., 2016. Response surface methodology: process and product optimization using designed experiments. John Wiley & Sons.
Nachouane, A., Abdelli, A., Friedrich, G., Vivier, S., 2016. Estimation of windage losses inside very narrow air gaps of high speed electrical machines without an internal ventilation using CFD methods. presented at the 2016 XXII International Conference on Electrical Machines (ICEM). IEEE, pp. 2704–2710.
Nakane, H., Okada, Y., Kosaka, T., Matsui, N., 2016. Experimental study on windage loss reduction using two types of rotor for hybrid excitation flux switching motor'. presented at the 2016 XXII International Conference on Electrical Machines (ICEM). IEEE, pp. 1707–1713.
Okada, Y., Kosaka, T., Matsui, N., 2017. Windage loss reduction for hybrid excitation flux switching motors based on rotor structure design. presented at the 2017 IEEE International Electric Machines and Drives Conference (IEMDC). IEEE, pp. 1–8.
Olabi, A.G., Wilberforce, T., Abdelkareem, M.A., Ramadan, M., 2021. Critical review of flywheel energy storage system. Energies 14 (8), 2159.
Pfister, P.-D., Perriard, Y., 2008. A 200 000 rpm, 2 kW slotless permanent magnet motor'. presented at the 2008 International Conference on Electrical Machines and Systems. IEEE, pp. 3054–3059.
L. Pokorny, N.J. Saikia, Y. Takeda, and E.J. Windhab, 'Influence of surface roughness on the flow behavior in TVF and WVF', presented at the Proceedings of the 10th International Symposium on Ultrasonic Doppler Methods for Fluid Mechanics and Fluid Engineering (ISUD 10), 10th International Symposium on Ultrasonic Doppler Methods for Fluid …, 2016, pp. 13–16.
Pullen, K.R., Dhand, A., 2014. '15 - Mechanical and electrical flywheel hybrid technology to store energy in vehicles'. In: Folkson, R. (Ed.), in Alternative Fuels and Advanced Vehicle Technologies for Improved Environmental Performance. Woodhead Publishing, pp. 476–504. https://doi.org/10.1533/9780857097422.2.476.
Reichardt, H., 1956. Über die Geschwindigkeitsverteilung in einer geradlinigen turbulenten Couetteströmung. ZAMM-J. Appl. Math. Mech. F. üR. Angew. Math. Mech. 36 (S1), S26–S29.
Reinke, P., Schmidt, M., Beckmann, T., 2018. The cavitating taylor-couette flow. Phys. Fluids 30 (10), 104101.
H. Ritchie, 'Cars, planes, trains: where do CO2 emissions from transport come from?', Oct. 2020. Accessed: Mar. 09, 2023. [Online]. Available: ⟨https://ourworldindata.org/co2-emissions-from-transport⟩.
Rohsenow, W.M., Hartnett, J.P., Cho, Y.I., 1998. Handbook of heat transfer, 3. Mcgraw-hill, New York.
Scheffe, H., 1999. The analysis of variance, 72. John Wiley & Sons.
Sun, B., Gu, T., Li, B., Wang, P., Gao, S., Wei, S., Nov. 2022. Design and application of electromechanical flywheel hybrid device for electric vehicle. Energy Rep. 8, 12570–12582. https://doi.org/10.1016/j.egyr.2022.09.078.
Suzuki, Y., Koyanagi, A., Kobayashi, M., Shimada, R., 2005. Novel applications of the flywheel energy storage system. Energy 30 (11–12), 2128–2143.
Tabatabaei, M., Lovison, A., Tan, M., Hartikainen, M., Miettinen, K., 2018. ANOVA-MOP: ANOVA decomposition for multiobjective optimization. SIAM J. Optim. 28 (4), 3260–3289.
Tachibana, F., Fukui, S., 1964. Convective heat transfer of the rotational and axial flow between two concentric cylinders. Bull. JSME 7 (26), 385–391.
Tatsumi, T., 2000. Turbulence as a complex mechanical-system. Appl. Energy 67 (1–2), 91–116.
Taylor, G.I., 1923. VIII. Stability of a viscous liquid contained between two rotating cylinders. Philos. Trans. R. Soc. Lond. Ser. Contain. Pap. Math. Phys. Character 223 (605–615), 289–343.
Tu, J., Yeoh, G.H., Liu, C., 2008. 'Chapter 3 - Governing Equations for CFD—Fundamentals. In: Tu, J., Yeoh, G.H., Liu, C. (Eds.), in Computational Fluid Dynamics. Butterworth-Heinemann, Burlington, pp. 65–125. https://doi.org/10.1016/B978-075068563-4.50005-7.
Verschoof, R.A., et al., 2018. Rough-wall turbulent taylor-couette flow: The effect of the rib height. Eur. Phys. J. E 41 (10), 1–9.
Walton, J.F., Heshmat, H., Tomaszewski, M., 2012. Power Loss in High-Speed Micro Turbomachinery: An Experimental Study. ', presented at the Turbo Expo: Power for Land, Sea, and Air. American Society of Mechanical Engineers, pp. 871–880.
Wang, W., Li, Y., Shi, M., Song, Y., Jul. 2021. Optimization and control of battery-flywheel compound energy storage system during an electric vehicle braking. Energy 226, 120404. https://doi.org/10.1016/j.energy.2021.120404.
Wang, B., Yu, X., Yang, X., Zhang, D., Nov. 2022. Control strategy for high speed flywheel energy storage system based on voltage threshold of DC1500 V transit transportation traction grid. 2022 4th Int. Conf. Clean. Energy Electr. Syst. 8, 640–647. https://doi.org/10.1016/j.egyr.2022.05.162.
Wen, C.-D., Mudawar, I., 2006. Modeling the effects of surface roughness on the emissivity of aluminum alloys. Int. J. Heat. Mass Transf. 49 (23–24), 4279–4289.
Zhang, J.W., Wang, Y.H., Liu, G.C., Tian, G.Z., Nov. 2022. A review of control strategies for flywheel energy storage system and a case study with matrix converter. Energy Rep. 8, 3948–3963. https://doi.org/10.1016/j.egyr.2022.03.009.
Zhang, Z., Yang, B., Zhang, Y., Li, L., Zhao, B., Zhang, T., Dec. 2023. Powertrain modeling and performance simulation of a novel flywheel hybrid electric vehicle. Energy Rep. 9, 4401–4412. https://doi.org/10.1016/j.egyr.2023.03.098.
Zhang, Y., Zhang, X., Qian, T., Hu, R., Dec. 2020. Modeling and simulation of a passive variable inertia flywheel for diesel generator. SIEnergy Storage - Driv. Clean. Energy Future 6, 58–68. https://doi.org/10.1016/j.egyr.2020.01.001.